

1 **^{231}Pa and ^{230}Th in the ocean model of the Community Earth System Model**
2 **(CESM1.3)**

3 Sifan Gu¹, Zhengyu Liu²

4
5 ¹Department of Atmospheric and Oceanic Sciences and Center for Climate Research,
6 University of Wisconsin-Madison, Madison, WI, USA

7 ²Atmospheric Science Program, Department of Geography, Ohio State University,
8 Columbus, OH, USA

9
10 Correspondence to: Sifan Gu (sgu28@wisc.edu)

11
12 Abstract

13 Sediment $^{231}\text{Pa}/^{230}\text{Th}$ activity ratio is emerging as an important proxy for
14 deep ocean circulation in the past. In order to allow for a direct model-data
15 comparison and to improve our understanding of sediment $^{231}\text{Pa}/^{230}\text{Th}$ activity
16 ratio, we implement ^{231}Pa and ^{230}Th in the ocean component of the Community
17 Earth System Model (CESM). In addition to the fully coupled implementation of the
18 scavenging behavior of ^{231}Pa and ^{230}Th with the active marine ecosystem module (p-
19 coupled), another form of ^{231}Pa and ^{230}Th have also been implemented with
20 prescribed particle flux fields of the present climate (p-fixed). The comparison of the
21 two forms of ^{231}Pa and ^{230}Th helps to isolate the influence of the particle fluxes from
22 that of ocean circulation. Under present day climate forcing, our model is able to
23 simulate water column ^{231}Pa and ^{230}Th activity and sediment $^{231}\text{Pa}/^{230}\text{Th}$ activity
24 ratio in good agreement with available observations. In addition, in response to
25 freshwater forcing, the p-coupled and p-fixed sediment $^{231}\text{Pa}/^{230}\text{Th}$ activity ratios
26 behave similarly over large areas of low productivity on long timescale, but can
27 differ substantially in some regions of high productivity and on short timescale,
28 indicating the importance of biological productivity in addition to ocean transport.
29 Therefore, our model provides a potentially powerful tool to help the interpretation
30 of sediment $^{231}\text{Pa}/^{230}\text{Th}$ reconstructions and to improve our understanding of past
31 ocean circulation and climate changes.

32 1. Introduction

33 Sediment $^{231}\text{Pa}/^{230}\text{Th}$ activity ratio has been one major proxy for ocean
34 circulation in the past (e.g. Yu et al. 1996; McManus et al. 2004; Gherardi et al.
35 2009). ^{231}Pa (32.5 ka half-life) and ^{230}Th (75.2 ka half-life) are produced at a
36 constant rate approximately uniformly in the ocean by the α decay of ^{235}U and ^{234}U ,
37 respectively, with a production activity ratio of 0.093 (Henderson and Anderson,
38 2003). Water column ^{231}Pa and ^{230}Th are subject to particle scavenging and
39 transport to sediments (Bacon and Anderson, 1982; Nozaki et al., 1987). Different
40 scavenging efficiency results in different ocean residence time: ^{231}Pa has a residence
41 time of approximately 111 years and ^{230}Th has a residence time of approximately 26
42 years (Yu et al., 1996). Longer residence time of ^{231}Pa than ^{230}Th makes ^{231}Pa more
43 subject to ocean transport and therefore in the modern ocean about 45% of ^{231}Pa
44 produced in the Atlantic is transported to the Southern Ocean (Yu et al., 1996),
45 resulting a lower than 0.093 sediment $^{231}\text{Pa}/^{230}\text{Th}$ activity ratio in the North Atlantic
46 and higher than 0.093 sediment $^{231}\text{Pa}/^{230}\text{Th}$ activity ratio in the Southern Ocean.

47 The application of the principle above to interpret sediment $^{231}\text{Pa}/^{230}\text{Th}$ as
48 the strength of Atlantic meridional overturning circulation (AMOC), however, can be
49 complicated by other factors, leading to uncertainties in using $^{231}\text{Pa}/^{230}\text{Th}$ as a proxy
50 for past circulation (Keigwin and Boyle, 2008; Lippold et al., 2009; Scholten et al.,
51 2008). In addition to the ocean transport, sediment $^{231}\text{Pa}/^{230}\text{Th}$ is also influenced by
52 particle flux and composition (Chase et al., 2002; Geibert and Usbeck, 2004;
53 Scholten et al., 2008; Siddall et al., 2007; Walter et al., 1997). The region of a higher
54 particle flux tends to have a higher $^{231}\text{Pa}/^{230}\text{Th}$ (Kumar et al., 1993; Yong Lao et al.,
55 1992), which is referred to as the “particle flux effect” (Siddall et al., 2005). Regional
56 high particle flux in the water column will favor the removal of isotopes into the
57 sediment, which leads to more isotopes transported into this region due to the
58 down-gradient diffusive flux and subsequently more removal of isotopes into the
59 sediment. Since ^{231}Pa has a longer residence time, this effect is more prominent on
60 ^{231}Pa than on ^{230}Th and therefore sediment $^{231}\text{Pa}/^{230}\text{Th}$ will be higher in high
61 productivity regions. Also, opal is able to scavenge ^{231}Pa much more effectively than
62 ^{230}Th , leading to higher $^{231}\text{Pa}/^{230}\text{Th}$ in high opal flux regions such as the Southern

63 Ocean (Chase et al., 2002). Moreover, sediment $^{231}\text{Pa}/^{230}\text{Th}$ is suggested to record
64 circulation change only within 1,000 m above the sediment, instead of the whole
65 water column, complicating the interpretation of sediment $^{231}\text{Pa}/^{230}\text{Th}$
66 reconstructions (Thomas et al., 2006). For example, sediment $^{231}\text{Pa}/^{230}\text{Th}$
67 approaching 0.093 during Heinrich Stadial event 1(HS1) from the subtropical North
68 Atlantic is interpreted as the collapse of AMOC (McManus et al., 2004). If sediment
69 $^{231}\text{Pa}/^{230}\text{Th}$ only records deepest water mass, it is possible that during HS1, AMOC
70 shoals, as opposed to a fully collapse, yet an increase of deep water imported from
71 the Southern Ocean featuring high $^{231}\text{Pa}/^{230}\text{Th}$ can increase the sediment
72 $^{231}\text{Pa}/^{230}\text{Th}$ approaching the production ratio (0.093) (Thomas et al., 2006).
73 Therefore, it is important to incorporate ^{231}Pa and ^{230}Th into climate models for a
74 direct model-data comparison and to promote a thorough understanding of
75 sediment $^{231}\text{Pa}/^{230}\text{Th}$ as well as past ocean circulation.

76 ^{231}Pa and ^{230}Th have been simulated in previous modeling studies (Dutay et al.,
77 2009; Luo et al., 2010; Marchal et al., 2000; Rempfer et al., 2017; Siddall et al.,
78 2005). Marchal et al., (2000) simulates ^{231}Pa and ^{230}Th in a zonally averaged
79 circulation model, using the reversible scavenging model of Bacon and Anderson,
80 (1982). One step further, Siddall et al. (2005) extends Marchal et al., (2000) by
81 including particle dissolution with prescribed particle export production in a 3-D
82 circulation model. Rempfer et al., (2017) further couples ^{231}Pa and ^{230}Th with active
83 biogeochemical model and includes boundary scavenging and sediment
84 resuspensions to improve model performance in simulating water column ^{231}Pa and
85 ^{230}Th activity. Here we follow previous studies to implement ^{231}Pa and ^{230}Th into the
86 Community Earth System Model (CESM). Our standard ^{231}Pa and ^{230}Th are coupled
87 with active marine ecosystem model (“p-coupled”) and therefore is influenced by
88 both ocean circulation change and particle flux change. To help to understand the
89 influence of the particle flux, we have also implemented an auxiliary version of
90 ^{231}Pa and ^{230}Th (“p-fixed”) for which the particle fluxes are fixed at prescribed
91 values. Therefore, p-fixed $^{231}\text{Pa}/^{230}\text{Th}$ is only influenced by ocean circulation change.
92 By comparing the p-fixed $^{231}\text{Pa}/^{230}\text{Th}$ with the p-coupled $^{231}\text{Pa}/^{230}\text{Th}$, we will be
93 able to separate the effect of circulation change from particle flux change. In

94 addition, the p-fixed ^{231}Pa and ^{230}Th can be run without the marine ecosystem
95 module, reducing computational cost by a factor of 3 in the ocean-alone model
96 simulation, making it a computationally efficient tracer for sensitivity studies.

97 This paper describes the details of ^{231}Pa and ^{230}Th in CESM and serves as a
98 reference for future studies using this tracer module. In section 2, we describe the
99 model and the implementation of ^{231}Pa and ^{230}Th . In sections 3, we describe the
100 experimental design. We will finally compare simulated ^{231}Pa and ^{230}Th fields with
101 observations, show model sensitivities on model parameter and also sediment
102 $^{231}\text{Pa}/^{230}\text{Th}$ ratio response to freshwater forcing in Section 4.

103

104 **2. Model Description**

105 2.1 Physical Ocean Model

106 We implement ^{231}Pa and ^{230}Th in the ocean model (Parallel Ocean Program
107 version 2, POP2) (Danabasoglu et al., 2012) of CESM (Hurrell et al., 2013). CESM is a
108 state-of-the-art coupled climate model and studies describing model components
109 and analyzing results can be found in a special collection in Journal of Climate
110 (<http://journals.ametsoc.org/topic/ccsm4-cesm1>). We run the ocean-alone model,
111 which is coupled to data atmosphere, land, ice and river runoff under the normal
112 year forcing of CORE-II data (Large and Yeager, 2008), using the low-resolution
113 version of POP2 with a nominal 3° horizontal resolution and 60 vertical layers.

114

115 2.2 Biogeochemical component (BGC)

116 CESM has incorporated a marine ecosystem module that simulates biological
117 variables (Moore et al., 2013). The marine ecosystem module has been validated
118 against present day observations extensively (e.g. Doney et al., 2009; Long et al.,
119 2013; Moore et al., 2002, 2004; Moore and Braucher, 2008). The implementation of
120 ^{231}Pa and ^{230}Th requires particle fields: CaCO_3 , opal and particulate organic carbon
121 (POC). These particle fields can be obtained through the ecosystem driver from the
122 ecosystem module (Jahn et al., 2015). The ecosystem module simulates the particle
123 fluxes in reasonable agreement with the present-day observations. The pattern and
124 magnitude of the annual mean particle fluxes (CaCO_3 , opal, POC) leaving the

125 euphotic zone at 105m are similar to the satellite observations (Fig. 7.2.5 and 9.2.2
 126 in Sarmiento and Gruber 2006) (Fig. 1 a~c): particle fluxes are higher in the high
 127 productivity regions such as high latitudes and equatorial Pacific; opal flux is high in
 128 the Southern Ocean. The remineralization scheme of particle is based on the ballast
 129 model of Armstrong et al., (2002). Detailed parameterizations for particle
 130 remineralization are documented in Moore et al., (2004) with temperature
 131 dependent remineralization length scales for POC and opal. We do not consider dust
 132 because it is suggested to be unimportant for ^{231}Pa and ^{230}Th fractionation (Chase et
 133 al., 2002; Siddall et al., 2005).

134

135 2.3 ^{231}Pa and ^{230}Th implementation

136 ^{231}Pa and ^{230}Th are produced from the α decay of ^{235}U and ^{234}U uniformly
 137 everywhere at constant rate β^i ($\beta^{\text{Pa}} = 2.33 \cdot 10^{-3} \text{ dpm m}^{-3} \text{ yr}^{-1}$, $\beta^{\text{Th}} = 2.52 \cdot 10^{-2} \text{ dpm m}^{-3}$
 138 yr^{-1}). ^{231}Pa and ^{230}Th are also subjective to radioactive decay with the decay
 139 constant of λ^i ($\lambda^{\text{Pa}} = 2.13 \cdot 10^{-5} \text{ yr}^{-1}$, $\lambda^{\text{Th}} = 9.22 \cdot 10^{-6} \text{ yr}^{-1}$).

140 Another important process contributes to ^{231}Pa and ^{230}Th activity is the
 141 reversible scavenging by sinking particles (Bacon and Anderson, 1982), which
 142 describes the adsorption of isotopes onto sinking particles and desorption after the
 143 dissolution of particles. This process transports ^{231}Pa and ^{230}Th downward and
 144 leads to a general increase of ^{231}Pa and ^{230}Th activity with depth. The reversible
 145 scavenging considers total isotope activity (A_t^i) as two categories (Eq. (1)):
 146 dissolved isotopes (A_d^i) and particulate isotopes (A_p^i) (superscript i refers to ^{231}Pa
 147 and ^{230}Th) and A_p^i is the sum of the isotopes associated with different particle types
 148 ($A_{j,p}^i$) (subscript j refers to different particle types: CaCO_3 , opal and POC):

$$149 \quad A_t^i = A_d^i + A_p^i = A_d^i + \sum_j A_{j,p}^i \quad (1)$$

150

151 Dissolved and particulate isotopes are assumed to be in equilibrium, which is a
 152 reasonable assumption in the open ocean (Bacon and Anderson, 1982; Henderson et

153 al., 1999; Moore and Hunter, 1985). The ratio between the particulate isotope
 154 activity and the dissolved isotope activity is set by a partition coefficient, K (Eq. (2)):

$$155 \quad K_j^i = \frac{A_{j,p}^i}{A_d^i \cdot R_j} \quad (2)$$

156

157 , where R_j is the ratio of particle concentration (C_j) to the density of seawater
 158 (1024.5 kg m^{-3}). Subscript j refers to different particle types (CaCO_3 , opal and POC).
 159 Values of partition coefficient K used in our control simulation follows Chase et al.,
 160 2002 and Siddall et al., 2005 (Table 2).

161 Particulate isotopes (A_p^i) will be transported by sinking particles, which is
 162 described by $w_s \frac{\partial A_p^i}{\partial z}$ (Eq. (3)), where w_s is the sinking velocity. We don't
 163 differentiate between slow sinking small particles and rapid sinking large particles
 164 as in Dutay et al., (2009) and consider all particles as slowly sinking small particles
 165 with sinking velocity of $w_s = 1000 \text{ m yr}^{-1}$ (Arsouze et al., 2009; Dutay et al., 2009;
 166 Kriest, 2002), which is similar to Rempfer et al., (2017) and Siddall et al., (2005).
 167 Any particulate isotopes (A_p^i) at the ocean bottom layer are removed from the
 168 ocean as sediment, which is the sink for the isotope budget. Detailed vertical
 169 differentiation scheme to calculate this term in the model is provided in the
 170 supplementary material. The reversible scavenging scheme applied here is the same
 171 as the neodymium implementation in POP2 (Gu et al., 2017).

172

173 Therefore, the conservation equation for ^{231}Pa and ^{230}Th activity can be
 174 written as

$$175 \quad \frac{\partial A_t^i}{\partial t} = \beta^i - \lambda^i A_t^i - w_s \frac{\partial A_p^i}{\partial z} + \text{Transport} \quad (3),$$

176 where the total isotope activity is controlled by decay from U (first term),
 177 radioactive decay (second term), reversible scavenging (third term) and physical
 178 transport by the ocean model (fourth term, including advection, convection and
 179 diffusion). A_p^i can be calculated by combining Eq. (1) and Eq. (2):

180 $A_t^i = A_d^i + A_d^i \cdot (K_{POC}^i \cdot R_{POC} + K_{CaCO_3}^i \cdot R_{CaCO_3} + K_{opal}^i \cdot R_{opal})$
 181 $= A_d^i \cdot (1 + K_{POC}^i \cdot R_{POC} + K_{CaCO_3}^i \cdot R_{CaCO_3} + K_{opal}^i \cdot R_{opal}),$ (4)

182 which leads to

183 $A_d^i = \frac{A_t^i}{1 + K_{POC}^i \cdot R_{POC} + K_{CaCO_3}^i \cdot R_{CaCO_3} + K_{opal}^i \cdot R_{opal}},$ (5)

184 put this back to Eq. (1), we get

185 $A_p^i = A_t^i \cdot \left(1 - \frac{1}{1 + K_{POC}^i \cdot R_{POC} + K_{CaCO_3}^i \cdot R_{CaCO_3} + K_{opal}^i \cdot R_{opal}}\right)$ (6)

186

187 Particle fields used in the reversible scavenging can be either prescribed or
 188 simultaneously generated from the marine ecosystem module. Therefore, two forms
 189 of ^{231}Pa and ^{230}Th are implemented in POP2: “p-fixed” and “p-coupled”. P-fixed ^{231}Pa
 190 and ^{230}Th use particle fluxes prescribed as annual mean particle fluxes generated
 191 from the marine ecosystem module under present day climate forcing (Fig.1). P-
 192 coupled ^{231}Pa and ^{230}Th use particle fluxes computed simultaneously from the
 193 marine ecosystem module. P-fixed and p-coupled ^{231}Pa and ^{230}Th can be turned on
 194 at the case build time and the p-coupled ^{231}Pa and ^{230}Th requires the ecosystem
 195 module to be turned on at the same time.

196

197 Comparing with previous studies of modeling ^{231}Pa and ^{230}Th , our p-fixed
 198 version is the same as Siddall et al., (2002), except that different prescribed particle
 199 fluxes are used. The p-coupled version allows coupling to biogeochemical module,
 200 which is similar to Rempfer et al., (2017), but we do not include boundary
 201 scavenging and sediment resuspensions as in Rempfer et al., (2017) because
 202 boundary scavenging and sediment resuspensions are suggested to be unimportant
 203 to influence the relationship between $^{231}\text{Pa}_p/^{230}\text{Th}_p$ and AMOC strength (Rempfer et
 204 al., 2017).

205

206 **3. Experiments**

207 We run a control experiment (CTRL) and two experiments with different
208 partition coefficients to show model sensitivity. We have both p-fixed and p-coupled
209 ^{231}Pa and ^{230}Th in CTRL, but only p-fixed ^{231}Pa and ^{230}Th in sensitivity experiments.
210 Equilibrium partition coefficients for ^{231}Pa and ^{230}Th vary among different particle
211 types and the magnitude of the partition coefficients for different particle types
212 remains uncertain (Chase et al., 2002; Chase and Robert F, 2004; Luo and Ku, 1999).
213 Since the control experiment in Siddall et al., (2005) is able to simulate major
214 features of ^{231}Pa and ^{230}Th distributions, we use the partition coefficients from the
215 control experiment in Siddall et al., (2005) in our CTRL (Table 2). Two sensitivity
216 experiments are performed with decreased (EXP_1) and increased (EXP_2) partition
217 coefficients by a factor of 5 (Table 2).

218 All the experiments are ocean-alone experiments with the normal year
219 forcing by CORE-II data (Large and Yeager, 2008). The ^{231}Pa and ^{230}Th activities are
220 initiated from 0 in CTRL and are integrated for 2,000 model years until equilibrium
221 is reached. EXP_1 and EXP_2 are initiated from 1,400 model year in CTRL and are
222 integrated for another 800 model years to reach equilibrium.

223 Since sediment $^{231}\text{Pa}/^{230}\text{Th}$ in North Atlantic has been used to reflect the
224 strength of AMOC, to test how sediment $^{231}\text{Pa}/^{230}\text{Th}$ in our model responds to the
225 change of AMOC and the change of particle fluxes, we carried out a fresh water
226 perturbation experiment (HOSING) with both p-fixed and p-coupled ^{231}Pa and ^{230}Th .
227 Starting from 2,000 model year of CTRL, a freshwater flux of 1 Sv is imposed over
228 the North Atlantic region of $50^\circ\text{N}\sim 70^\circ\text{N}$ and the experiment is integrated for 1400
229 model years until both p-fixed and p-coupled sediment $^{231}\text{Pa}/^{230}\text{Th}$ ratio have
230 reached quasi-equilibrium. The partition coefficients used in HOSING are the same
231 as in CTRL.

232

233 **4. Results**

234 4.1 Control Experiment

235 P-fixed and p-coupled version of ^{231}Pa and ^{230}Th in CTRL show identical
236 results (Fig. 2-4). P-fixed and p-coupled dissolved and particulate ^{231}Pa and ^{230}Th in
237 CTRL are highly correlated with each other with correlations greater than 0.995 and

238 regression coefficients are all near 1.0 ($R^2 > 0.995$). The correlation coefficient
239 between p-fixed and p-coupled sediment $^{231}\text{Pa}/^{230}\text{Th}$ activity ratios in CTRL is 0.99
240 and the regression coefficient is 0.9 ($R^2 = 0.98$). This is expected because the particle
241 fields used in p-fixed version are prescribed as the climatology of the particle fields
242 used in the p-coupled version. Therefore, under the same climate forcing, p-fixed
243 and p-coupled version of ^{231}Pa and ^{230}Th should be very similar. For the discussion
244 of results in CTRL below, we only discuss the p-fixed ^{231}Pa and ^{230}Th .

245 The residence time of both ^{231}Pa and ^{230}Th in CTRL are comparable with
246 observations. The residence time is calculated as the ratio of global average total
247 isotope activity and the radioactive ingrowth of the isotope. Residence time in CTRL
248 is 118 yr for ^{231}Pa and 33 yr for ^{230}Th (Table 2), which are of the same magnitude as
249 111 yr for ^{231}Pa and 26 yr for ^{230}Th in observation (Yu et al., 1996).

250 CTRL can simulate the general features of dissolved water column ^{231}Pa and
251 ^{230}Th activities. Dissolved ^{231}Pa and ^{230}Th activities increase with depth in CTRL, as
252 shown in two GEOTRACES transects (Deng et al., 2014; Hayes et al., 2015) in the
253 Atlantic (Fig. 2 and 3). The dissolved ^{231}Pa and ^{230}Th activities in CTRL are also at
254 the same order of magnitude as in observations in the most of the ocean, except that
255 simulated values are larger than observations in the abyssal, which is also the case
256 in Siddall et al., (2005) and Rempfer et al., (2017) (their Fig. 2 and 3, experiment
257 Re3d). Our model is unable to simulate the realistic dissolved ^{231}Pa and ^{230}Th
258 activities in the abyssal probably because boundary scavenging and sediment
259 resuspensions are not included in our model. In Rempfer et al., 2017, without
260 boundary scavenging and sediment resuspension, dissolved ^{231}Pa and ^{230}Th
261 activities are quite large in the deep ocean. However, if boundary scavenging and
262 sediment resuspension are included, the water column dissolved ^{231}Pa and ^{230}Th
263 activity is in the right magnitude compared with observation. Therefore, we hypothesize
264 that with boundary scavenging and sediment resuspensions added, dissolved ^{231}Pa
265 and ^{230}Th activities in the abyssal should be greatly reduced.

266 A more quantitative model-data comparison is shown in Fig. 5. The linear
267 regression coefficient between model results and observations (references of
268 observations are listed in Table 3), an indication of model ability to simulate ^{231}Pa

269 and ^{230}Th activity (Dutay et al., 2009), is near 1.0 for dissolved ^{231}Pa and ^{230}Th (1.02
270 for $[\text{}^{231}\text{Pa}]_d$ and 1.14 for $[\text{}^{230}\text{Th}]_d$), suggesting that CTRL can simulate the dissolved
271 ^{231}Pa and ^{230}Th in good agreement with observations. However, the simulation of
272 the particulate activity is not as good as the dissolved activity. Particulate activity is
273 overall larger than observation in the surface ocean and smaller than observation in
274 the deep ocean for both particulate ^{231}Pa and ^{230}Th . The regression coefficient for
275 particulate ^{231}Pa and ^{230}Th is 0.02 for $[\text{}^{231}\text{Pa}]_p$ and 0.05 for $[\text{}^{230}\text{Th}]_p$. The poor
276 performance in simulating water column particulate ^{231}Pa and ^{230}Th activities is also
277 in previous modeling studies (Dutay et al., 2009; Siddall et al., 2005), because of
278 similar modelling scheme applied. However, the simulated $^{231}\text{Pa}_p/^{230}\text{Th}_p$ is in
279 reasonable agreement with observations. The $^{231}\text{Pa}_p/^{230}\text{Th}_p$ along two GEOTRACES
280 transects (Fig. 2 and 3) show the similar pattern and magnitude as in Rempfer et al.,
281 (2017), consistent with observations. Decrease of $^{231}\text{Pa}_p/^{230}\text{Th}_p$ with depth is well
282 simulated, which is suggested to be caused by the lateral transport of ^{231}Pa from
283 North Atlantic to Southern Ocean by AMOC (Gherardi et al., 2009; Lippold et al.,
284 2011, 2012a; Luo et al., 2010; Rempfer et al., 2017).

285 The sediment $^{231}\text{Pa}/^{230}\text{Th}$ in CTRL is overall consistent with observations
286 (references of observations are listed in Table 3). The North Atlantic shows low
287 sediment $^{231}\text{Pa}/^{230}\text{Th}$ activity ratio as in observations because ^{231}Pa is more subject
288 to the southward transport by active ocean circulation than ^{230}Th because of its
289 longer residence time. The Southern Ocean maximum in the sediment $^{231}\text{Pa}/^{230}\text{Th}$
290 activity ratio is also simulated in CTRL. High opal fluxes in the Southern Ocean,
291 which preferentially removes ^{231}Pa into sediment ($K_{opal}^{231Pa} > K_{opal}^{230Th}$) (Chase et al.,
292 2002), leading to increased sediment $^{231}\text{Pa}/^{230}\text{Th}$ activity ratio. In addition,
293 upwelling in the Southern Ocean brings up deep water enriched with ^{231}Pa , which is
294 transported from the North Atlantic, to shallower depth and further contribute to
295 the scavenging. CTRL can also produce higher sediment $^{231}\text{Pa}/^{230}\text{Th}$ activity ratio in
296 regions with high particle production (e.g. the Eastern equatorial Pacific, the North
297 Pacific and the Indian Ocean) due to the “particle flux effect”. Specifically, in North
298 Atlantic, the distribution of sediment $^{231}\text{Pa}/^{230}\text{Th}$ matches the distribution of

299 particle, especially opal, production: sediment $^{231}\text{Pa}/^{230}\text{Th}$ is higher where opal
300 production is high, and vice versa (Fig. 4 and Fig. 1c). Quantitatively, the regression
301 coefficient between sediment $^{231}\text{Pa}/^{230}\text{Th}$ in CTRL and observation in the Atlantic is
302 0.86, which is larger than in other basins. This suggests that sediment $^{231}\text{Pa}/^{230}\text{Th}$ is
303 better simulated in the Atlantic than in other basins. One possible explanation is that
304 sediment $^{231}\text{Pa}/^{230}\text{Th}$ in the Atlantic is controlled by both ocean circulation and
305 particle flux, while in other basins sediment $^{231}\text{Pa}/^{230}\text{Th}$ is controlled almost only by
306 particle flux. With active AMOC, the north south gradient of sediment $^{231}\text{Pa}/^{230}\text{Th}$
307 can be simulated. However, for example, in the Southern Ocean, sediment
308 $^{231}\text{Pa}/^{230}\text{Th}$ is dominantly controlled by opal flux, which varies on small scales and is
309 difficult for simulation. Therefore, model performance in simulating sediment
310 $^{231}\text{Pa}/^{230}\text{Th}$ in the Southern Ocean is not as good as in the Atlantic.

311

312 4.2 Sensitivity on partition coefficient K

313 In this section, we show model sensitivity on partition coefficient by
314 increasing and decreasing the partition coefficient, K, by a factor of 5, but keeping
315 the relative ratio for different particles the same (Table 2). Our model shows similar
316 model sensitivity as in Siddall et al., (2005) as discussed below.

317 As stated in Siddall et al., (2005), the isotope decay term in Eq. (3) is three
318 orders of magnitude less than the production term. If we neglect the transport term
319 and the decay term in Eq. (3) and assume particulate phase activity at the surface as
320 0, when reach equilibrium, the activity of particulate phase will be as in Eq. (7). Eq.
321 (7) combined with Eq. (2) and $R_i = \frac{F}{w_s * \rho}$, we can obtain Eq. (8). Under the
322 assumption that there is isotope decay and ocean transport, Eq. (7) suggests that the
323 particulate isotope activity depends on the production rate and settling velocity and
324 will increase linearly with depth. Eq. (8) suggests that the dissolved isotope activity
325 depends on the production rate, partition coefficient K and particle flux and will also
326 increase linearly with depth. Any departure from this linear relationship with depth
327 is due to ocean transport, which is suggested by observations (Bacon and Anderson,

328 1982; Roy-Barman et al., 1996). Results of Eq. (7) and Eq. (8) can help to understand
329 the differences in Exp_1 and Exp_2.

330 Increasing K will decrease water column dissolved ^{231}Pa and ^{230}Th activities
331 but won't change particulate ^{231}Pa and ^{230}Th too much (Fig. 6). Magnitude of
332 dissolved ^{231}Pa and ^{230}Th in Exp_1 (smaller K) is at least one order larger than that
333 in Exp_2 (larger K), while magnitude of particulate ^{231}Pa and ^{230}Th in Exp_1 and
334 Exp_2 is in the same order. As suggested by Eq. (8), if there is no isotope decay and
335 no ocean transport, larger K will lead to smaller dissolved isotope activity but
336 unchanged particulate activity. Intuitively, larger K will lead to more ^{231}Pa and ^{230}Th
337 attached to particles and further buried into sediment, which increases the sink for
338 the ^{231}Pa and ^{230}Th budget. With the sources for ^{231}Pa and ^{230}Th staying the same,
339 dissolved ^{231}Pa and ^{230}Th will be reduced. Increasing K will also reduce the vertical
340 gradient of dissolved ^{231}Pa and ^{230}Th as reversible scavenging act as the vertical
341 transport and increase this vertical transport can decrease the vertical gradient.
342 However, changes in the particulate ^{231}Pa and ^{230}Th is relatively small (Fig. 6). Eq.
343 (7) suggests that particulate phase activity it is independent of K. Therefore,
344 changing K will have limited influence on particulate phase activity.

$$345 \quad A_p^i(z) = \frac{\beta^i}{w_s} \cdot z \quad (7)$$

$$346 \quad A_d^i(z) = \frac{\rho\beta^i}{K^i F} \cdot z \quad (8)$$

347

348 Increasing K will also reduce the spatial gradient in sediment $^{231}\text{Pa}/^{230}\text{Th}$
349 activity ratio and vice versa (Fig. 7). Larger K will decrease the ^{231}Pa and ^{230}Th
350 residence time and most isotopes produced in the water column are removed into
351 sediment locally (Table 2). Therefore, sediment $^{231}\text{Pa}/^{230}\text{Th}$ ratio becomes more
352 homogeneous and approaching the production ration of 0.093 (Fig. 7b). The
353 deviation (the root mean squared error) of sediment $^{231}\text{Pa}/^{230}\text{Th}$ is 0.0726 in CTRL,
354 0.0770 in Exp_1 and 0.0739 in Exp_2. The linear regression coefficients between
355 sediment $^{231}\text{Pa}/^{230}\text{Th}$ in the model and the observations are listed in Table S1 in the

356 supplementary information. Although the performance of global sediment
357 $^{231}\text{Pa}/^{230}\text{Th}$ in Exp_1 is better than CTRL, the performance of Atlantic $^{231}\text{Pa}/^{230}\text{Th}$ in
358 Exp_1 is worse. We consider better simulating sediment $^{231}\text{Pa}/^{230}\text{Th}$ in the Atlantic
359 is more important since the most important application of sediment $^{231}\text{Pa}/^{230}\text{Th}$ is
360 using sediment $^{231}\text{Pa}/^{230}\text{Th}$ in the North Atlantic to reconstruct past AMOC. In
361 addition, water column isotope activity is too large in Exp_1 compared with
362 observation. Therefore, the partition coefficient in CTRL is of the right order of
363 magnitude.

364

365 4.3. Sediment $^{231}\text{Pa}/^{230}\text{Th}$ ratio in HOSING

366 Potential changes in the export of biogenic particles makes using $^{231}\text{Pa}/^{230}\text{Th}$
367 ratio to reconstructing AMOC strength under debate. In response to freshwater
368 perturbation in the North Atlantic, both biological productivity and AMOC strength
369 will change and will influence sediment $^{231}\text{Pa}/^{230}\text{Th}$ in different ways. Our model
370 with p-fixed and p-coupled ^{231}Pa and ^{230}Th can help to detangle these two effects. In
371 this section, we examine the sediment $^{231}\text{Pa}/^{230}\text{Th}$ (p-fixed and p-coupled) response
372 in the North Atlantic to idealized fresh water perturbation.

373 In HOSING, after applying freshwater forcing to the North Atlantic, AMOC
374 strength quickly decreases to a minimum of 2 Sv (AMOC_off) (Fig. 9a). During the
375 AMOC_off state, compared with CTRL with active AMOC (AMOC_on), p-fixed
376 sediment $^{231}\text{Pa}/^{230}\text{Th}$ shows an overall increase in the North Atlantic and a decrease
377 in the South Atlantic (Fig. 10b) because of the reduced southward transport of ^{231}Pa
378 from the North Atlantic by AMOC, consistent with paleo proxy evidence there (e.g.
379 Gherardi et al., 2005, 2009; McManus et al., 2004). The overall increase of sediment
380 $^{231}\text{Pa}/^{230}\text{Th}$ ratio in the North Atlantic in response to the AMOC collapse can be seen
381 more clearly in the time evolution of the sediment $^{231}\text{Pa}/^{230}\text{Th}$ ratio averaged from
382 20°N to 60°N in the North Atlantic (Fig.9b, green). Quantitatively, the $^{231}\text{Pa}/^{230}\text{Th}$
383 increases from 0.074 in AMOC_on to 0.098 in AMOC_off in the p-fixed version,
384 approaching the production ration of 0.093. This increase of $^{231}\text{Pa}/^{230}\text{Th}$ is also in
385 the subtropical North Atlantic from the two sites near Bermuda Rise (Fig. 9e and f),
386 which is of comparable magnitude with the change from LGM to HS1 in

387 reconstructions there (McManus et al., 2004). In addition, the pattern of p-fixed
388 (Fig.10a) sediment $^{231}\text{Pa}/^{230}\text{Th}$ ratio during the Atlantic in AMOC_off state is similar
389 to the opal distribution (Fig.1b) because, without active circulation, sediment
390 $^{231}\text{Pa}/^{230}\text{Th}$ ratio is more controlled by particle flux effect, which is similar to the
391 Pacific in CTRL. It is further noted that our p-fixed sediment $^{231}\text{Pa}/^{230}\text{Th}$ ratio in
392 HOSING behaves similarly to that in Siddall et al., (2007).

393 The overall increase in p-fixed sediment $^{231}\text{Pa}/^{230}\text{Th}$ ratio in the North
394 Atlantic is not homogenous and the magnitude of the change between AMOC_on and
395 AMOC_off varies with location, depending on the distribution of particle flux,
396 especially the opal flux (Fig.9 and 10). The maximum increase in p-fixed sediment
397 $^{231}\text{Pa}/^{230}\text{Th}$ ratio occurs near 40°N western Atlantic (Fig. 10a), where the opal
398 production in our model is maximum in North Atlantic (Fig. 1b). The sediment
399 $^{231}\text{Pa}/^{230}\text{Th}$ ratio in this region during AMOC_on is larger than production ratio of
400 0.093 because opal maximum provides extra ^{231}Pa to this region (“particle flux
401 effect”), which overwhelms the active ocean circulation transporting ^{231}Pa
402 southward outside this region (Fig. 9d, green). During AMOC_off, without active
403 ocean circulation, the particle flux effect becomes even stronger because less ^{231}Pa is
404 transported out of the North Atlantic and p-fixed sediment $^{231}\text{Pa}/^{230}\text{Th}$ ratio
405 becomes even larger. It should be noted that the opal maximum in this region is not
406 in the observation (Fig. 7.2.5 in Sarmiento and Gruber 2006). However, our
407 sediment $^{231}\text{Pa}/^{230}\text{Th}$ response in HOSING is self-consistent with the particle flux in
408 our model since the location of maximum $^{231}\text{Pa}/^{230}\text{Th}$ increase matches the location
409 of opal flux in our model.

410 In most regions of the Atlantic, p-coupled sediment $^{231}\text{Pa}/^{230}\text{Th}$ shows a
411 similar response to p-fixed $^{231}\text{Pa}/^{230}\text{Th}$ in HOSING. The evolution of p-fixed and p-
412 coupled sediment $^{231}\text{Pa}/^{230}\text{Th}$ activity ratio in HOSING are highly correlated (Fig.
413 11a). The change of sediment $^{231}\text{Pa}/^{230}\text{Th}$ ratio from AMOC_on to AMOC_off are
414 similar in both p-fixed and p-coupled version (Fig.11b). The correlation between p-
415 fixed and p-coupled sediment $^{231}\text{Pa}/^{230}\text{Th}$ ratio change from AMOC_on to AMOC_off
416 is 0.72 (1455points) and the linear regression coefficient is 0.71 ($R^2 = 0.52$). High
417 correlation between p-fixed and p-coupled response mainly happens over low

418 productivity regions (Fig.1, 10, and 11), where circulation effect on sediment
419 $^{231}\text{Pa}/^{230}\text{Th}$ is more important than the particle flux change in HOSING.

420 In spite of these similarities discussed above, the responses of p-fixed and p-
421 coupled sediment $^{231}\text{Pa}/^{230}\text{Th}$ to the fresh water forcing can differ significantly in
422 high productivity regions because of the productivity change. With persistent
423 freshwater forcing over the North Atlantic, most regions in the North Atlantic show
424 reduced production of CaCO_3 , opal and POC (Fig. 8). Productivity in the North
425 Atlantic is suggested to be halved during AMOC collapse because of increased
426 stratification, which reduces nutrient supply from deep ocean (Schmittner, 2005). In
427 our model, the productivity in the mid-latitude North Atlantic is indeed greatly
428 reduced after the freshwater forcing is applied. For example, opal production from
429 30°N - 50°N in the Atlantic at the end of HOSING is reduced by 50%~90% of its
430 original value in CTRL. However, opal production increases in high latitude North
431 Atlantic (north of 50°N). The pattern of opal production changes with high opal
432 production region shifts northward in HOSING (Fig. 8 d, e and f). These particle flux
433 changes will influence sediment $^{231}\text{Pa}/^{230}\text{Th}$ as discussed below.

434 North of 50°N in the Atlantic, the opal productivity increases during
435 AMOC_off (Fig. 8f) and will result an increase in sediment $^{231}\text{Pa}/^{230}\text{Th}$. The increase
436 caused by greater opal productivity enhances the sediment $^{231}\text{Pa}/^{230}\text{Th}$ increase
437 caused by reduced AMOC. Therefore, the increase in p-coupled sediment $^{231}\text{Pa}/^{230}\text{Th}$
438 from AMOC_on to AMOC_off is larger than p-fixed sediment $^{231}\text{Pa}/^{230}\text{Th}$ change
439 (Fig.9c).

440 In the mid-latitude North Atlantic, the opal productivity decreases during
441 AMOC_off (Fig.8 f) and will lead to a decrease in sediment $^{231}\text{Pa}/^{230}\text{Th}$, which is
442 opposite to the effect of reduced AMOC. P-coupled sediment $^{231}\text{Pa}/^{230}\text{Th}$ shows an
443 initial decrease in first 200 years (Fig.9 d, e, and f, red dash lines) caused by the
444 reduced opal productivity. But this decrease trend is reversed eventually, suggesting
445 that the influence of particle flux change is overwhelmed by the effect of reduced
446 AMOC. In the long run, most regions in the subtropical and mid-latitude Atlantic
447 show increased sediment $^{231}\text{Pa}/^{230}\text{Th}$ in HOSING (Fig.10 d), indicating the dominant
448 effect of reduced AMOC. However, sediment $^{231}\text{Pa}/^{230}\text{Th}$ at 40°N west Atlantic,

449 where opal productivity is maximum during AMOC_on, show a decrease from
450 AMOC_on to AMOC_off (Fig.9 d and Fig.10 d). During AMOC_on, the opal productivity
451 maximum at 40°N west Atlantic lead to regional maximum sediment $^{231}\text{Pa}/^{230}\text{Th}$
452 because of the particle flux effect (Fig. 4). During AMOC_off, this opal productivity
453 maximum is eliminated (Fig.8 e) and there is no more extra ^{231}Pa supplied by
454 surroundings to this region, which leads to a decrease in sediment $^{231}\text{Pa}/^{230}\text{Th}$. This
455 decrease in sediment $^{231}\text{Pa}/^{230}\text{Th}$ caused by productivity change is greater than the
456 increase caused by the reduced AMOC. Therefore, sediment $^{231}\text{Pa}/^{230}\text{Th}$ experiences
457 a decrease from AMOC_on to AMOC_off at this location (Fig.9 d and Fig.10 d). Our
458 results suggest that although the circulation effect is more dominant than the
459 particle flux change in controlling sediment $^{231}\text{Pa}/^{230}\text{Th}$ on long time scale over
460 most of North Atlantic (Fig. 11), particle flux change can be important on short time
461 scale and in high productivity regions. With p-fixed and p-coupled ^{231}Pa and ^{230}Th ,
462 our model can help to detangle the circulation effect and particle flux effect.

463

464 It has been suggested that the particulate $^{231}\text{Pa}/^{230}\text{Th}$ response to the change
465 of AMOC depends on the location and depth. Above 2km and high latitude North
466 Atlantic, particulate $^{231}\text{Pa}/^{230}\text{Th}$ decreases with the increased AMOC (Rempfer et al.,
467 2017). Our results are consistent with this finding (Fig. 12 a and b). Both p-fixed and
468 p-coupled particulate $^{231}\text{Pa}/^{230}\text{Th}$ show similar patterns of change from AMOC_on to
469 AMOC_off: decrease in particulate $^{231}\text{Pa}/^{230}\text{Th}$ at shallow depth and north of 60°N
470 and increase in particulate $^{231}\text{Pa}/^{230}\text{Th}$ below 2km and south of 60°N during
471 AMOC_off. Therefore, sediment depth should also be taken into consideration when
472 interpreting sediment $^{231}\text{Pa}/^{230}\text{Th}$. Since the pattern in p-coupled is similar to the
473 pattern in p-fixed, the opposite particulate $^{231}\text{Pa}/^{230}\text{Th}$ changes in shallow and deep
474 North Atlantic is associated with AMOC change. During AMOC_on, upper limb of
475 AMOC (about upper 1km) transport water northward, which provides extra ^{231}Pa to
476 North Atlantic and particulate $^{231}\text{Pa}/^{230}\text{Th}$ is larger than the production ratio of
477 0.093. In contrast, the lower limb of AMOC (2km-3km) features southward
478 transport, which transports ^{231}Pa to the Southern Ocean and particulate $^{231}\text{Pa}/^{230}\text{Th}$
479 is smaller than the production ratio of 0.093 (Fig. 12 solid). Particulate $^{231}\text{Pa}/^{230}\text{Th}$

480 decreases with depth (Fig. 12 c solid). During AMOC_off, ocean transport of ^{231}Pa is
481 greatly reduced. Therefore, shallow (deep) depth experiences a decrease (increase)
482 in particulate $^{231}\text{Pa}/^{230}\text{Th}$ and the vertical gradient in the particulate $^{231}\text{Pa}/^{230}\text{Th}$ is
483 also greatly reduced (Fig. 12 c dash). Our results support that the depth dependence
484 of particulate $^{231}\text{Pa}/^{230}\text{Th}$ is mainly caused by lateral transport of ^{231}Pa by
485 circulation (Gherardi et al., 2009; Lippold et al., 2011, 2012a; Luo et al., 2010;
486 Rempfer et al., 2017).

487 Overall, our model is able to simulate the correct magnitude of the sediment
488 $^{231}\text{Pa}/^{230}\text{Th}$ ratio response to the freshwater forcing. Our experiments suggest that
489 the change of circulation is the dominant factor that influences sediment
490 $^{231}\text{Pa}/^{230}\text{Th}$ on long time scale over most of the globe in the idealized hosing
491 experiment, although the detailed difference between p-fixed and p-coupled
492 sediment $^{231}\text{Pa}/^{230}\text{Th}$ ratio response to freshwater forcing in different locations can
493 be complicated.

494

495

496 **5. Summary**

497 ^{231}Pa and ^{230}Th have been implemented in the ocean model of the CESM in
498 both the p-coupled and p-fixed forms. Our control experiment under present day
499 climate forcing is able to simulate most ^{231}Pa and ^{230}Th water column activity and
500 sediment $^{231}\text{Pa}/^{230}\text{Th}$ activity ratio consistent with observations by using the
501 parameters that are suggested by Chase et al., (2002) and used in Siddall et al.
502 (2005). Our sensitivity experiments with varying parameters suggest that these
503 parameters are of the right order of magnitude.

504 Furthermore, our model is able to simulate the overall sediment $^{231}\text{Pa}/^{230}\text{Th}$
505 ratio change in the North Atlantic with a magnitude comparable to the
506 reconstruction in response to the collapse of AMOC, although the detailed response
507 can be complicated in different regions. Finally, the p-fixed form is able to capture
508 many major features of that of the p-coupled form over large ocean areas on long
509 time scale, although the two forms can also differ significantly in some regions,
510 especially the region with high opal productivity.

511 Much remains to be improved in our ^{231}Pa and ^{230}Th module in the future.
512 For example, the model can be further improved by including nepheloid layers to
513 better simulate water column ^{231}Pa and ^{230}Th activity as in Rempfer et al. (2017). In
514 addition, partition coefficient for different particles can be further tuned , which can
515 improve our understanding of the affinity of ^{231}Pa and ^{230}Th to different particles,
516 complementing the limited observational studies available (e.g. Chase et al., 2002;
517 Scholten et al., 2005; Walter et al., 1997). At present, as the first attempt to implement
518 ^{231}Pa and ^{230}Th in the CESM with both p-fixed and p-coupled versions, our model
519 can serve as a useful tool to improve our understanding of the processes of ^{231}Pa
520 and ^{230}Th as well as interpretations of sediment $^{231}\text{Pa}/^{230}\text{Th}$ reconstructions for past
521 ocean circulation and climate changes.

522

523

524 **Code availability:**

525 The ^{231}Pa and ^{230}Th isotope source code of both p-fixed and p-coupled versions for
526 CESM1.3 is included as supplementary material here.

527

528

529 **Acknowledgement:**

530 This work is supported by NSF P2C2 program (NSF 1401778 and NSF1600080),
531 DOE DE-SC0006744 and NSFC 41630527 and 41130105. Computing resources
532 (ark:/85065/d7wd3xhc) were provided by the Climate Simulation Laboratory at
533 NCAR's Computational and Information Systems Laboratory, sponsored by the
534 National Science Foundation and other agencies.

535

536 **References:**

537 Anderson, R. F., Bacon, M. P. and Brewer, P. G.: Removal of ^{230}Th and ^{231}Pa from the
538 open ocean, *Earth Planet. Sci. Lett.*, 62(1), 7–23, doi:10.1016/0012-821X(83)90067-
539 5, 1983.
540 Anderson, R. F., Lao, Y., Broecker, W. S., Trumbore, S. E., Hofmann, H. J. and Wolfli, W.:
541 Boundary scavenging in the Pacific Ocean: A comparison of ^{10}Be and ^{231}Pa , *Earth*
542 *Planet. Sci. Lett.*, 96(3–4), 287–304, doi:10.1016/j.cognition.2008.05.007, 1990.
543 Anderson, R. F., Fleisher, M. Q., Biscaye, P. E., Kumar, N., Dittrich, B., Kubik, P. and
544 Suter, M.: Anomalous boundary scavenging in the Middle Atlantic Bight: evidence

545 from ^{230}Th , ^{231}Pa , ^{10}Be and ^{210}Pb , *Deep. Res. Part II*, 41(2-3), 537-561,
546 doi:10.1016/0967-0645(94)90034-5, 1994.

547 Armstrong, R. A., Lee, C., Hedges, J. I., Honjo, S. and Wakeham, S. G.: A new,
548 mechanistic model for organic carbon fluxes in the ocean based on the quantitative
549 association of POC with ballast minerals, *Deep. Res. Part II Top. Stud. Oceanogr.*,
550 49(1-3), 219-236, doi:10.1016/S0967-0645(01)00101-1, 2002.

551 Arsouze, T., Dutay, J.-C., Lacan, F. and Jeandel, C.: Reconstructing the Nd oceanic
552 cycle using a coupled dynamical – biogeochemical model, *Biogeosciences*, 6(12),
553 2829-2846, doi:10.5194/bg-6-2829-2009, 2009.

554 Bacon, M. and Anderson, R.: Distribution of Thorium Isotopes between dissolved
555 and particulate forms in the deep sea, *J. Geophys. Res. ...*, 87(1), 2045-2056, 1982.

556 Bacon, M. P. and Rosholt, J. N.: Accumulation rates of ^{230}Th , ^{231}Pa , and some
557 transition metals on the Bermuda Rise, *Geochim. Cosmochim. Acta*, 46, 651-666,
558 1982.

559 Bacon, M. P., Huh, C. A. and Moore, R. M.: Vertical profiles of some natural
560 radionuclides over the Alpha Ridge, Arctic Ocean, *Earth Planet. Sci. Lett.*, 95(1-2),
561 15-22, doi:10.1016/0012-821X(89)90164-7, 1989.

562 Bradtmiller, L. I., Anderson, R. F., Fleisher, M. Q. and Burckle, L. H.: Opal burial in the
563 equatorial Atlantic Ocean over the last 30 ka: Implications for glacial-interglacial
564 changes in the ocean silicon cycle, *Paleoceanography*, 22(4), 1-15,
565 doi:10.1029/2007PA001443, 2007.

566 Bradtmiller, L. I., McManus, J. F. and Robinson, L. F.: $^{231}\text{Pa}/^{230}\text{Th}$ evidence for a
567 weakened but persistent Atlantic meridional overturning circulation during
568 Heinrich Stadial 1, *Nat. Commun.*, 5, 5817, doi:10.1038/ncomms6817, 2014.

569 Burckel, P., Waelbroeck, C., Luo, Y., Roche, D. M., Pichat, S., Jaccard, S. L., Gherardi, J.,
570 Govin, A., Lippold, J. and Thil, F.: Changes in the geometry and strength of the
571 Atlantic meridional overturning circulation during the last glacial (20-50 ka), *Clim.*
572 *Past*, 12(11), 2061-2075, doi:10.5194/cp-12-2061-2016, 2016.

573 Chase, Z. and Robert F, A.: Comment on “On the importance of opal, carbonate, and
574 lithogenic clays in scavenging and fractionating ^{230}Th , ^{231}Pa and ^{10}Be in the ocean”
575 by S. Luo and T.-L. Ku, *Earth Planet. Sci. Lett.*, 220(1-2), 201-211,
576 doi:10.1016/S0012-821X(04)00027-5, 2004.

577 Chase, Z., Anderson, R. F., Fleisher, M. Q. and Kubik, P. W.: The influence of particle
578 composition and particle flux on scavenging of Th, Pa and Be in the ocean, *Earth*
579 *Planet. Sci. Lett.*, 204(1-2), 215-229, doi:10.1016/S0012-821X(02)00984-6, 2002.

580 Cochran, J. K., Livingston, H. D., Hirschberg, D. J. and Surprenant, L. D.: Natural and
581 anthropogenic radionuclide distributions in the northwest Atlantic Ocean, *Earth*
582 *Planet. Sci. Lett.*, 84(2-3), 135-152, doi:10.1016/0012-821X(87)90081-1, 1987.

583 Cochran, J. K., Hirschberg, D. J., Livingston, H. D., Buesseler, K. O. and Key, R. M.:
584 Natural and anthropogenic radionuclide distributions in the Nansen Basin, Arctic
585 Ocean: Scavenging rates and circulation timescales, *Deep. Res. Part II*, 42(6), 1495-
586 1517, doi:10.1016/0967-0645(95)00051-8, 1995.

587 Colley, S., Thomson, J. and Newton, P. P.: Detailed Th-230, Th-232 and Pb-210 fluxes
588 recorded by the 1989/90 BOFS sediment trap time-series at 48N, 20W, *Deep - Sea*
589 *Res. Part I - Oceanogr. Res. Pap.*, 42(6), 833-848, 1995.

590 Coppola, L., Roy-Barman, M., Mulsow, S., Povinec, P. and Jeandel, C.: Thorium

591 isotopes as tracers of particles dynamics and deep water circulation in the Indian
592 sector of the Southern Ocean (ANTARES IV), *Mar. Chem.*, 100(3–4 SPEC. ISS.), 299–
593 313, doi:10.1016/j.marchem.2005.10.019, 2006.

594 Danabasoglu, G., Bates, S. C., Briegleb, B. P., Jayne, S. R., Jochum, M., Large, W. G.,
595 Peacock, S. and Yeager, S. G.: The CCSM4 ocean component, *J. Clim.*, 25(5), 1361–
596 1389, doi:10.1175/JCLI-D-11-00091.1, 2012.

597 DeMaster, D. J.: *The marine budgets of silica and ³²Si*, Yale., 1979.

598 Deng, F., Thomas, A. L., Rijkenberg, M. J. A. and Henderson, G. M.: Controls on
599 seawater ²³¹Pa, ²³⁰Th and ²³²Th concentrations along the flow paths of deep
600 waters in the Southwest Atlantic, *Earth Planet. Sci. Lett.*, 390, 93–102,
601 doi:10.1016/j.epsl.2013.12.038, 2014.

602 Doney, S. C., Lima, I., Feely, R. A., Glover, D. M., Lindsay, K., Mahowald, N., Moore, J. K.
603 and Wanninkhof, R.: Mechanisms governing interannual variability in upper-ocean
604 inorganic carbon system and air-sea CO₂ fluxes: Physical climate and atmospheric
605 dust, *Deep. Res. Part II Top. Stud. Oceanogr.*, 56(8–10), 640–655,
606 doi:10.1016/j.dsr2.2008.12.006, 2009.

607 Dutay, J.-C., Lacan, F., Roy-Barman, M. and Bopp, L.: Influence of particle size and
608 type on ²³¹Pa and ²³⁰Th simulation with a global coupled biogeochemical-ocean
609 general circulation model: A first approach, *Geochemistry, Geophys. Geosystems*,
610 10(1), doi:10.1029/2008GC002291, 2009.

611 Edmonds, H. N., Moran, S. B., Hoff, J. A., Smith, J. N. and Edwards, R. L.: Protactinium-
612 ²³¹ and Thorium-²³⁰ Abundances and High Scavenging Rates in the Western Arctic
613 Ocean, *Science* (80-.), 280(5362), 405–407, doi:10.1126/science.280.5362.405,
614 1998.

615 Edmonds, H. N., Moran, S. B., Cheng, H. and Edwards, R. L.: ²³⁰Th and ²³¹Pa in the
616 Arctic Ocean: Implications for particle fluxes and basin-scale Th/Pa fractionation,
617 *Earth Planet. Sci. Lett.*, 227(1–2), 155–167, doi:10.1016/j.epsl.2004.08.008, 2004.

618 Francois, R., Bacon, M. P., Altabet, M. A. and Labeyrie, L. D.: Glacial/interglacial
619 changes in sediment rain rate in the SW Indian Sector of subantarctic Waters as
620 recorded by ²³⁰Th, ²³¹Pa, U, and δ¹⁵N, *Paleoceanography*, 8(5), 611–629,
621 doi:10.1029/93PA00784, 1993.

622 Frank, M.: Reconstruction of Late Quaternary environmental conditions applying the
623 natural radionuclides ²³⁰Th, ¹⁰Be, ²³¹Pa and ²³⁸U: A study of deep-sea sediments
624 from the eastern sector of the Antarctic Circumpolar Current System, Alfred
625 Wegener Institute for Polar and Marine Research., 1996.

626 Frank, M., Eisenhauer, A., Kubik, P. W., Ditttrich-hannen, B. and Segl, M.: Beryllium ¹⁰,
627 thorium ²³⁰, and protactinium ²³¹ in Galapagos microplate sediments:
628 Implications of hydrothermal activity and paleoproductivity changes during the last
629 100,000 years, *Palaeogeography*, 9(4), 559–578, 1994.

630 Geibert, W. and Usbeck, R.: Adsorption of thorium and protactinium onto different
631 particle types: Experimental findings, *Geochim. Cosmochim. Acta*, 68(7), 1489–1501,
632 doi:10.1016/j.gca.2003.10.011, 2004.

633 Gherardi, J., Labeyrie, L., Mcmanus, J., Francois, R., Skinner, L. and Cortijo, E.:
634 Evidence from the Northeastern Atlantic basin for variability in the rate of the
635 meridional overturning circulation through the last deglaciation, *Earth Planet. Sci.*
636 *Lett.*, 240(3–4), 710–723, doi:10.1016/j.epsl.2005.09.061, 2005.

637 Gherardi, J.-M., Labeyrie, L., Nave, S., Francois, R., McManus, J. F. and Cortijo, E.:
638 Glacial-interglacial circulation changes inferred from $^{231}\text{Pa}/^{230}\text{Th}$ sedimentary
639 record in the North Atlantic region, *Paleoceanography*, 24(2),
640 doi:10.1029/2008PA001696, 2009.

641 Gu, S., Liu, Z., Zhang, J., Rempfer, J., Joos, J., Brady, E. and Oppo, D.: Coherent response
642 of Antarctic Intermediate Water and Atlantic Meridional Overturning Circulation
643 during the last deglaciation, *Palaeogeography*, doi:10.1002/2017PA003092, 2017.

644 Guo, L., Santschi, P. H., Baskaran, M. and Zindler, A.: Distribution of dissolved and
645 particulate ^{230}Th and ^{232}Th in seawater from the Gulf of Mexico and off Cape
646 Hatteras as measured by SIMS, *Earth Planet. Sci. Lett.*, 133(1), 117–128, 1995.

647 Gutjahr, M., Frank, M., Stirling, C. H., Keigwin, L. D. and Halliday, a. N.: Tracing the Nd
648 isotope evolution of North Atlantic Deep and Intermediate Waters in the western
649 North Atlantic since the Last Glacial Maximum from Blake Ridge sediments, *Earth
650 Planet. Sci. Lett.*, 266(1–2), 61–77, doi:10.1016/j.epsl.2007.10.037, 2008.

651 Hall, I. R., Moran, S. B., Zahn, R., Knutz, P. C., Shen, C.-C. and Edwards, R. L.:
652 Accelerated drawdown of meridional overturning in the late-glacial Atlantic
653 triggered by transient pre-H event freshwater perturbation, *Geophys. Res. Lett.*,
654 33(16), L16616, doi:10.1029/2006GL026239, 2006.

655 Hayes, C. T., Anderson, R. F., Fleisher, M. Q., Serno, S., Winckler, G. and Gersonde, R.:
656 Quantifying lithogenic inputs to the North Pacific Ocean using the long-lived
657 thorium isotopes, *Earth Planet. Sci. Lett.*, 383, 16–25,
658 doi:10.1016/j.epsl.2013.09.025, 2013.

659 Hayes, C. T., Anderson, R. F., Fleisher, M. Q., Huang, K. F., Robinson, L. F., Lu, Y., Cheng,
660 H., Edwards, R. L. and Moran, S. B.: ^{230}Th and ^{231}Pa on GEOTRACES GA03, the U.S.
661 GEOTRACES North Atlantic transect, and implications for modern and
662 paleoceanographic chemical fluxes, *Deep. Res. Part II Top. Stud. Oceanogr.*, 116, 29–
663 41, doi:10.1016/j.dsr2.2014.07.007, 2015.

664 Henderson, G. M. and Anderson, R. F.: The U-series toolbox for paleoceanography,
665 *Rev. Mineral. Geochemistry*, 52(1), 493–531, doi:10.2113/0520493, 2003.

666 Henderson, G. M., Heinze, C., Anderson, R. F. and Winguth, A. M. E.: Global
667 distribution of the ^{230}Th flux to ocean sediments constrained by GCM modelling,
668 *Deep. Res. Part I Oceanogr. Res. Pap.*, 46(11), 1861–1893, doi:10.1016/S0967-
669 0637(99)00030-8, 1999.

670 Hoffmann, S. S., McManus, J. F., Curry, W. B. and Brown-Leger, L. S.: Persistent export
671 of ^{231}Pa from the deep central Arctic Ocean over the past 35,000 years., *Nature*,
672 497(7451), 603–6, doi:10.1038/nature12145, 2013.

673 Hsieh, Y. Te, Henderson, G. M. and Thomas, A. L.: Combining seawater ^{232}Th and
674 ^{230}Th concentrations to determine dust fluxes to the surface ocean, *Earth Planet.
675 Sci. Lett.*, 312(3–4), 280–290, doi:10.1016/j.epsl.2011.10.022, 2011.

676 Huh, C. A. and Beasley, T. M.: Profiles of dissolved and particulate thorium isotopes
677 in the water column of coastal Southern California, *Earth Planet. Sci. Lett.*, 85(1–3),
678 1–10, doi:10.1016/0012-821X(87)90016-1, 1987.

679 Hurrell, J. W., Holland, M. M., Gent, P. R., Ghan, S., Kay, J. E., Kushner, P. J., Lamarque, J.
680 F., Large, W. G., Lawrence, D., Lindsay, K., Lipscomb, W. H., Long, M. C., Mahowald, N.,
681 Marsh, D. R., Neale, R. B., Rasch, P., Vavrus, S., Vertenstein, M., Bader, D., Collins, W. D.,
682 Hack, J. J., Kiehl, J. and Marshall, S.: The community earth system model: A

683 framework for collaborative research, *Bull. Am. Meteorol. Soc.*, 94(9), 1339–1360,
684 doi:10.1175/BAMS-D-12-00121.1, 2013.

685 Jahn, A., Lindsay, K., Giraud, X., Gruber, N., Otto-Bliesner, B. L., Liu, Z. and Brady, E. C.:
686 Carbon isotopes in the ocean model of the Community Earth System Model (CESM1),
687 *Geosci. Model Dev.*, 8(8), 2419–2434, doi:10.5194/gmd-8-2419-2015, 2015.

688 Jonkers, L., Zahn, R., Thomas, A., Henderson, G., Abouchami, W., Francois, R.,
689 Masque, P., Hall, I. R. and Bickert, T.: Deep circulation changes in the central South
690 Atlantic during the past 145 kyrs reflected in a combined $^{231}\text{Pa}/^{230}\text{Th}$,
691 Neodymium isotope and benthic $\delta^{13}\text{C}$ record, *Earth Planet. Sci. Lett.*, 419, 14–21,
692 doi:10.1016/j.epsl.2015.03.004, 2015.

693 Keigwin, L. D. and Boyle, E. A.: Did North Atlantic overturning halt 17,000 years ago?,
694 *Paleoceanography*, 23(1), 1–5, doi:10.1029/2007PA001500, 2008.

695 Kriest, I.: Different parameterizations of marine snow in a 1D-model and their
696 influence on representation of marine snow, nitrogen budget and sedimentation,
697 *Deep. Res. Part I Oceanogr. Res. Pap.*, 49(12), 2133–2162, doi:10.1016/S0967-
698 0637(02)00127-9, 2002.

699 Ku, T. L.: Uranium series disequilibrium in deep sea sediments, Columbia., 1966.

700 Ku, T. L., Bischoff, J. L. and Boersma, A.: Age studies of Mid-Atlantic Ridge sediments
701 near 42°N and 20°N , *Deep. Res. Oceanogr. Abstr.*, 19(3), 233–247,
702 doi:10.1016/0011-7471(72)90033-2, 1972.

703 Kumar, N.: Trace metals and natural radionuclides as tracers of ocean productivity,
704 Columbia., 1994.

705 Kumar, N., Gwiazda, R., Anderson, R. F. and Froelich, P. N.: $^{231}\text{Pa}/^{230}\text{Th}$ ratios in
706 sediments as a proxy for past changes in Southern Ocean productivity, *Nature*, 362,
707 45–48, doi:10.1038/362045a0, 1993.

708 Large, W. G. and Yeager, S. G.: The global climatology of an interannually varying air-
709 sea flux data set, *Clim. Dyn.*, 33(2–3), 341–364, doi:10.1007/s00382-008-0441-3,
710 2008.

711 Lippold, J., Grützner, J., Winter, D., Lahaye, Y., Mangini, A. and Christi, M.: Does
712 sedimentary $^{231}\text{Pa}/^{230}\text{Th}$ from the Bermuda Rise monitor past Atlantic Meridional
713 Overturning Circulation?, *Geophys. Res. Lett.*, 36(12), 1–6,
714 doi:10.1029/2009GL038068, 2009.

715 Lippold, J., Gherardi, J. M. and Luo, Y.: Testing the $^{231}\text{Pa}/^{230}\text{Th}$ paleocirculation proxy:
716 A data versus 2D model comparison, *Geophys. Res. Lett.*, 38(20), 1–7,
717 doi:10.1029/2011GL049282, 2011.

718 Lippold, J., Mulitza, S., Mollenhauer, G., Weyer, S., Heslop, D. and Christl, M.:
719 Boundary scavenging at the East Atlantic margin does not negate use of $^{231}\text{Pa}/$
720 ^{230}Th to trace Atlantic overturning, *Earth Planet. Sci. Lett.*, 333–334, 317–331,
721 doi:10.1016/j.epsl.2012.04.005, 2012a.

722 Lippold, J., Luo, Y., Francois, R., Allen, S. E., Gherardi, J., Pichat, S., Hickey, B. and
723 Schulz, H.: Strength and geometry of the glacial Atlantic Meridional Overturning
724 Circulation, *Nat. Geosci.*, 5(11), 813–816, doi:10.1038/ngeo1608, 2012b.

725 Long, M. C., Lindsay, K., Peacock, S., Moore, J. K. and Doney, S. C.: Twentieth-century
726 oceanic carbon uptake and storage in CESM1(BGC), *J. Clim.*, 26(18), 6775–6800,
727 doi:10.1175/JCLI-D-12-00184.s1, 2013.

728 Luo, S. and Ku, T. L.: Oceanic $^{231}\text{Pa}/^{230}\text{Th}$ ratio influenced by particle composition

729 and remineralization, *Earth Planet. Sci. Lett.*, 167(3–4), 183–195,
730 doi:10.1016/S0012-821X(99)00035-7, 1999.

731 Luo, S. D., Ku, T. L., Kusakabe, M., Bishop, J. K. B. and Yang, Y. L.: Tracing particle
732 cycling in the upper ocean with Th-230 and Th-228: An investigation in the
733 equatorial Pacific along 140 degrees W, *Deep - Sea Res. Part II - Top. Stud. Oceanogr.*,
734 42(2–3), 805–829, doi:10.1016/0967-0645(95)00019-M, 1995.

735 Luo, Y., Francois, R. and Allen, S.: Sediment ²³¹Pa/²³⁰Th as a recorder of the rate of
736 the Atlantic meridional overturning circulation: insights from a 2-D model, *Ocean
737 Sci.*, 6(3), 381–400, doi:10.5194/os-6-381-2010, 2010.

738 Mangini, A. and Diester-Hass, L.: Excess Th-230 in sediments off NW Africa traces
739 upwelling during the past 130,000 years, in *Coastal upwelling: Its sedimentary
740 records*, edited by E. Suess and J. Thiede, pp. 455–470, Plenum., 1983.

741 Mangini, A. and Key, R. M.: A ²³⁰Th profile in the Atlantic Ocean, *Earth Planet. Sci.
742 Lett.*, 62(3), 377–384, doi:10.1016/0012-821X(83)90008-0, 1983.

743 Mangini, A. and Sonntag, C.: ²³¹Pa dating of deep-sea cores via ²²⁷Th counting,
744 *Earth Planet. Sci. Lett.*, 37(2), 251–256, 1977.

745 Mangini, A. and U., K.: Depositional history in the Clarion-Clipperton zone during the
746 last 250,000 years: ²³⁰Th and ²³¹Pa methods, *Geol. Jahrb.*, 87, 105–121, 1987.

747 Marchal, O., François, R., Stocker, T. F. and Joos, F.: Ocean thermohaline circulation
748 and sedimentary ²³¹Pa/²³⁰Th ratio, *Paleoceanography*, 15(6), 625–641 [online]
749 Available from: <http://onlinelibrary.wiley.com/doi/10.1029/2000PA000496/full>
750 (Accessed 19 April 2016), 2000.

751 McManus, J., Francois, R. and Gherardi, J.: Collapse and rapid resumption of Atlantic
752 meridional circulation linked to deglacial climate changes, *Nature*, 428(6985), 834–
753 837, 2004.

754 Moore, J. K. and Braucher, O.: Sedimentary and mineral dust sources of dissolved
755 iron to the World Ocean, *Biogeosciences*, 5(1994), 631–656, doi:10.5194/bgd-4-
756 1279-2007, 2008.

757 Moore, J. K., Doney, S. C., Glover, D. M. and Fung, I. Y.: Iron cycling and nutrient-
758 limitation patterns in surface waters of the World Ocean, , 49, 463–507, 2002.

759 Moore, J. K., Doney, S. C. and Lindsay, K.: Upper ocean ecosystem dynamics and iron
760 cycling in a global three-dimensional model, *Global Biogeochem. Cycles*, 18(4),
761 doi:10.1029/2004GB002220, 2004.

762 Moore, J. K., Lindsay, K., Doney, S. C., Long, M. C. and Misumi, K.: Marine Ecosystem
763 Dynamics and Biogeochemical Cycling in the Community Earth System Model
764 [CESM1(BGC)]: Comparison of the 1990s with the 2090s under the RCP4.5 and
765 RCP8.5 Scenarios, *J. Clim.*, 26(23), 9291–9312, doi:10.1175/JCLI-D-12-00566.1,
766 2013.

767 Moore, R. M. and Hunter, K. A.: Thorium adsorption in the ocean: reversibility and
768 distribution amongst particle sizes, *Geochim. Cosmochim. Acta*, 49(11), 2253–2257,
769 doi:10.1016/0016-7037(85)90225-X, 1985.

770 Moore, W. S.: The thorium isotope content of ocean water, *Earth Planet. Sci. Lett.*,
771 53(3), 419–426, doi:10.1016/0012-821X(81)90046-7, 1981.

772 Moran, S. B., Hoff, J. A., Buesseler, K. O. and Edwards, R. L.: High precision ²³⁰Th and
773 ²³²Th in the Norwegian Sea and Denmark by thermal ionization mass
774 spectrometry, , 22(19), 2589–2592, 1995.

775 Moran, S. B., Charette, M. a., Hoff, J. a., Edwards, R. L. and Landing, W. M.: Distribution
776 of ^{230}Th in the Labrador Sea and its relation to ventilation, *Earth Planet. Sci. Lett.*,
777 150, 151–160, doi:10.1016/S0012-821X(97)00081-2, 1997.

778 Moran, S. B., Shen, C.-C., Weinstein, S. E., Hettlinger, L. H., Hoff, J. H., Edmonds, H. N.
779 and Edwards, R. L.: Constraints on deep water age and particle flux in the Equatorial
780 and South Atlantic Ocean based on seawater ^{231}Pa and ^{230}Th data, *Geophys. Res.*
781 *Lett.*, 28(18), 3437–3440 [online] Available from:
782 papers2://publication/uuid/2A811583-B32B-4BD8-B582-EC8B0D96A949, 2001.

783 Moran, S. B., Shen, C. C., Edmonds, H. N., Weinstein, S. E., Smith, J. N. and Edwards, R.
784 L.: Dissolved and particulate ^{231}Pa and ^{230}Th in the Atlantic Ocean: Constraints on
785 intermediate/deep water age, boundary scavenging, and $^{231}\text{Pa}/^{230}\text{Th}$
786 fractionation, *Earth Planet. Sci. Lett.*, 203(3–4), 999–1014, doi:10.1016/S0012-
787 821X(02)00928-7, 2002.

788 Müller, P. J. and Mangini, A.: Organic carbon decomposition rates in sediments of the
789 pacific manganese nodule belt dated by ^{230}Th and ^{231}Pa , *Earth Planet. Sci. Lett.*,
790 51(1), 94–114, doi:10.1016/0012-821X(80)90259-9, 1980.

791 Negre, C., Zahn, R., Thomas, A. L., Masqué, P., Henderson, G. M., Martínez-Méndez, G.,
792 Hall, I. R. and Mas, J. L.: Reversed flow of Atlantic deep water during the Last Glacial
793 Maximum., *Nature*, 468(7320), 84–88, doi:10.1038/nature09508, 2010.

794 Nozaki, Y. and Horibe, Y.: Alpha-emitting thorium isotopes in northwest Pacific deep
795 waters, *Earth Planet. Sci. Lett.*, 65(1), 39–50, doi:10.1016/0012-821X(83)90188-7,
796 1983.

797 Nozaki, Y. and Nakanishi, T.: ^{231}Pa and ^{230}Th profiles in the open ocean water
798 column, *Deep Sea Res. Part A, Oceanogr. Res. Pap.*, 32(10), 1209–1220,
799 doi:10.1016/0198-0149(85)90004-4, 1985.

800 Nozaki, Y. and Yamada, M.: Thorium and protactinium isotope distributions in
801 waters of the Japan Sea, *Deep Sea Res. Part A, Oceanogr. Res. Pap.*, 34(8), 1417–1430,
802 1987.

803 Nozaki, Y. and Yang, H. S.: Th and Pa isotopes in the waters of the western margin of
804 the pacific near Japan: Evidence for release of ^{228}Ra and ^{227}Ac from slope
805 sediments, *J. Oceanogr. Soc. Japan*, 43(4), 217–227, doi:10.1007/BF02109817, 1987.

806 Nozaki, Y., Horibe, Y. and Tsubota, H.: The water column distribution of thorium
807 isotopes in the western North Pacific, *Earth Planet. Sci. Lett.*, 54(54), 203–216, 1981.

808 Nozaki, Y., Yang, H.-S. and Yamada, M.: Scavenging of thorium in the ocean, *J.*
809 *Geophys. Res.*, 92(C1), 772, doi:10.1029/JC092iC01p00772, 1987.

810 Okubo, A., Obata, H., Nozaki, Y., Yamamoto, Y. and Minami, H.: ^{230}Th in the
811 Andaman Sea: Rapid deep-sea renewal, *Geophys. Res. Lett.*, 31(22), 1–5,
812 doi:10.1029/2004GL020226, 2004.

813 Okubo, A., Obata, H., Luo, S., Gamo, T., Yamamoto, Y., Minami, H. and Yamada, M.:
814 Particle flux in the twilight zone of the eastern Indian Ocean: A constraint from
815 ^{234}U - ^{230}Th and ^{228}Ra - ^{228}Th disequilibria, *Deep. Res. Part I Oceanogr. Res. Pap.*,
816 54(10), 1758–1772, doi:10.1016/j.dsr.2007.06.009, 2007a.

817 Okubo, A., Obata, H., Gamo, T., Minami, H. and Yamada, M.: Scavenging of ^{230}Th in
818 the Sulu Sea, *Deep. Res. Part II Top. Stud. Oceanogr.*, 54(1–2), 50–59,
819 doi:10.1016/j.dsr2.2006.02.016, 2007b.

820 Okubo, A., Obata, H., Gamo, T. and Yamada, M.: ^{230}Th and ^{232}Th distributions in

821 mid-latitudes of the North Pacific Ocean: Effect of bottom scavenging, *Earth Planet.*
822 *Sci. Lett.*, 339–340, 139–150, doi:10.1016/j.epsl.2012.05.012, 2012.

823 Rempfer, J., Stocker, T. F., Joos, F., Lippold, J. and Jaccard, S. L.: New insights into
824 cycling of ^{231}Pa and ^{230}Th in the Atlantic Ocean, *Earth Planet. Sci. Lett.*, 468, 27–
825 37, doi:10.1016/j.epsl.2017.03.027, 2017.

826 Roberts, N. L., McManus, J. F., Piotrowski, A. M. and McCave, I. N.: Advection and
827 scavenging controls of Pa/Th in the northern NE Atlantic, *Paleoceanography*, 29(6),
828 668–679, doi:10.1002/2014PA002633, 2014.

829 Robinson, L. F., Belshaw, N. S. and Henderson, G. M.: U and Th concentrations and
830 isotope ratios in modern carbonates and waters from the Bahamas, *Geochim.*
831 *Cosmochim. Acta*, 68(8), 1777–1789, doi:10.1016/j.gca.2003.10.005, 2004.

832 Roy-Barman, M., Chen, J. H. and Wasserburg, G. J.: ^{230}Th - ^{232}Th systematics in the
833 central Pacific Ocean: The sources and the fates of thorium, *Earth Planet. Sci. Lett.*,
834 139(3–4), 351–363, doi:10.1016/0012-821X(96)00017-9, 1996.

835 Rutgers van der Loeff, M. M. and Berger, G. W.: Scavenging of ^{230}Th and ^{231}Pa near
836 the antarctic polar front in the South Atlantic, *Deep. Res. Part I*, 40(2), 339–357,
837 doi:10.1016/0967-0637(93)90007-P, 1993.

838 Schmittner, A.: Decline of the marine ecosystem caused by a reduction in the
839 Atlantic overturning circulation., *Nature*, 434(7033), 628–633,
840 doi:10.1038/nature03476, 2005.

841 Schmitz, W., Mangini, A., Stoffers, P., Glasby, G. P. and Pluger, W. L.: Sediment
842 accumulation rates in the southwestern Pacific Basin and Aitutaki Passage, *Mar.*
843 *Geol.*, 73(1), 181–190, 1986.

844 Scholten, J. C., Rutgers van der Loeff, M. M. and Michel, A.: Distribution of ^{230}Th and
845 ^{231}Pa in the water column in relation to the ventilation of the deep Arctic basins,
846 *Deep. Res. Part II*, 42(6), 1519–1531, doi:10.1016/0967-0645(95)00052-6, 1995.

847 Scholten, J. C., Fietzke, J., Mangini, A., Stoffers, P., Rixen, T., Gaye-Haake, B., Blanz, T.,
848 Ramaswamy, V., Sirocko, F., Schulz, H. and Ittekkot, V.: Radionuclide fluxes in the
849 Arabian Sea: The role of particle composition, *Earth Planet. Sci. Lett.*, 230(3–4), 319–
850 337, doi:10.1016/j.epsl.2004.11.003, 2005.

851 Scholten, J. C., Fietzke, J., Mangini, A., Garbe-Schönberg, C. D., Eisenhauer, A.,
852 Schneider, R. and Stoffers, P.: Advection and scavenging: Effects on ^{230}Th and
853 ^{231}Pa distribution off Southwest Africa, *Earth Planet. Sci. Lett.*, 271(1–4), 159–169,
854 doi:10.1016/j.epsl.2008.03.060, 2008.

855 Shimmiel, G. B. and Price, N. B.: The scavenging of U, ^{230}Th and ^{231}Pa during
856 pulsed hydrothermal activity at 20°S, East Pacific Rise, *Geochim. Cosmochim. Acta*,
857 52(3), 669–677, doi:10.1016/0016-7037(88)90329-8, 1988.

858 Shimmiel, G. B., Murray, J. W., Thomson, J., Bacon, M. P., Anderson, R. F. and Price, N.
859 B.: The distribution and behaviour of ^{230}Th and ^{231}Pa at an ocean margin, Baja
860 California, Mexico, *Geochim. Cosmochim. Acta*, 50(11), 2499–2507,
861 doi:10.1016/0016-7037(86)90032-3, 1986.

862 Siddall, M., Henderson, G. M., Edwards, N. R., Frank, M., Müller, S. a., Stocker, T. F. and
863 Joos, F.: $^{231}\text{Pa}/^{230}\text{Th}$ fractionation by ocean transport, biogenic particle flux and
864 particle type, *Earth Planet. Sci. Lett.*, 237(1–2), 135–155,
865 doi:10.1016/j.epsl.2005.05.031, 2005.

866 Siddall, M., Stocker, T. F., Henderson, G. M., Joos, F., Frank, M., Edwards, N. R., Ritz, S.

867 P. and Müller, S. a.: Modeling the relationship between $^{231}\text{Pa}/^{230}\text{Th}$ distribution
868 in North Atlantic sediment and Atlantic meridional overturning circulation,
869 *Paleoceanography*, 22(2), n/a-n/a, doi:10.1029/2006PA001358, 2007.
870 Thomas, A. L., Henderson, G. M. and Robinson, L. F.: Interpretation of the
871 $^{231}\text{Pa}/^{230}\text{Th}$ paleocirculation proxy: New water-column measurements from the
872 southwest Indian Ocean, *Earth Planet. Sci. Lett.*, 241(3-4), 493-504,
873 doi:10.1016/j.epsl.2005.11.031, 2006.
874 Trimble, S. M., Baskaran, M. and Porcelli, D.: Scavenging of thorium isotopes in the
875 Canada Basin of the Arctic Ocean, *Earth Planet. Sci. Lett.*, 222(3-4), 915-932,
876 doi:10.1016/j.epsl.2004.03.027, 2004.
877 Venchiarutti, C., van der Loeff, M. R. and Stimac, I.: Scavenging of ^{231}Pa and thorium
878 isotopes based on dissolved and size-fractionated particulate distributions at Drake
879 Passage (ANTXXIV-3), *Deep. Res. Part II Top. Stud. Oceanogr.*, 58(25-26), 2767-
880 2784, doi:10.1016/j.dsr2.2010.10.040, 2011.
881 Vogler, S., Scholten, J., Rutgers van der Loeff, M. M. and Mangini, A.: ^{230}Th in the
882 eastern North Atlantic: the importance of water mass ventilation in the balance of
883 ^{230}Th , *Earth Planet. Sci. Lett.*, 156(1-2), 61-74, doi:10.1016/S0012-
884 821X(98)00011-9, 1998.
885 Walter, H. J., Rutgers van der Loeff, M. M. and Hoeltzen, H.: Enhanced scavenging of
886 ^{231}Pa relative to ^{230}Th in the South Atlantic south of the Polar Front: Implications
887 for the use of the $^{231}\text{Pa}/^{230}\text{Th}$ ratio as a paleoproductivity proxy, *Earth Planet. Sci.*
888 *Lett.*, 149(1), 85-100, doi:10.1016/S0012-821X(97)00068-X, 1997.
889 Yang, H. S., Nozaki, Y., Sakai, H. and Masuda, A.: The distribution of ^{230}Th and ^{231}Pa
890 in the deep-sea surface sediments of the Pacific Ocean, *Geochim. Cosmochim. Acta*,
891 50(1), 81-89, doi:10.1016/0016-7037(86)90050-5, 1986.
892 Yong-Liang Yang, Elderfield, H., Pedersen, T. F. and Ivanovich, M.: Geochemical
893 record of the Panama Basin during the Last Glacial Maximum carbon event shows
894 that the glacial ocean was not suboxic, *Geology*, 23(12), 1115-1118,
895 doi:10.1130/0091-7613(1995)023<1115:GROTPB>2.3.CO, 1995.
896 Yong Lao, Anderson, R. F., Broecker, W. S., Trumbore, S. E., Hofmann, H. J. and Wolfli,
897 W.: Transport and burial rates of ^{10}Be and ^{231}Pa in the Pacific Ocean during the
898 Holocene period, *Earth Planet. Sci. Lett.*, 113(1-2), 173-189, doi:10.1016/0012-
899 821X(92)90218-K, 1992.
900 Yu, E.-F.: Variations in the Particulate Flux of ^{230}Th and ^{231}Pa and
901 Paleoceanographic Applications of the $^{231}\text{Pa}/^{230}\text{Th}$ Ratio, WHOI/MIT., 1994.
902 Yu, E.-F., Francois, R. and Bacon, M. P.: Similar rates of modern and last-glacial ocean
903 thermohaline circulation inferred from radiochemical data, *Nature*, 379(6567),
904 689-694, doi:10.1038/379689a0, 1996.
905

Variable	Symbol	Value	Units
Production of ^{231}Pa from U decay	β^{Pa}	$2.33 \cdot 10^{-3}$	$\text{dpm m}^{-3} \text{ yr}^{-1}$
Production of ^{230}Th from U decay	β^{Th}	$2.52 \cdot 10^{-2}$	$\text{dpm m}^{-3} \text{ yr}^{-1}$
Decay constant of ^{231}Pa	λ^{Pa}	$2.13 \cdot 10^{-5}$	yr^{-1}
Decay constant of ^{230}Th	λ^{Th}	$9.22 \cdot 10^{-6}$	yr^{-1}
Index for ^{231}Pa and ^{230}Th	i		
Index for particle type	j		
Total isotope activity	A_t		dpm m^{-3}
Dissolved isotope activity	A_d		dpm m^{-3}
Particle associated activity	A_p		dpm m^{-3}
Particle settling velocity	w_s	1000	m yr^{-1}
Particle concentration	C		kg m^{-3}
Density of seawater		1024.5	kg m^{-3}
Ratio between particle concentration and density of seawater	R		

906 Table 1. List of parameters, abbreviations and values.

907

908

	CTRL		EXP_1		EXP_2	
	^{231}Pa	^{230}Th	^{231}Pa	^{230}Th	^{231}Pa	^{230}Th
K_{CaCO_3}	$2.5 \cdot 10^5$	$1.0 \cdot 10^7$	$5 \cdot 10^4$	$2 \cdot 10^6$	$1.25 \cdot 10^6$	$5 \cdot 10^7$
K_{Opal}	$1.67 \cdot 10^6$	$5 \cdot 10^5$	$3.33 \cdot 10^5$	$1 \cdot 10^5$	$8.33 \cdot 10^6$	$2.5 \cdot 10^6$
K_{POC}	$1.0 \cdot 10^7$	$1.0 \cdot 10^7$	$2 \cdot 10^6$	$2 \cdot 10^6$	$5 \cdot 10^7$	$5 \cdot 10^7$
τ (yr)	118	33	501	143	27	9

909 Table 2. Partition coefficients for different particle types and residence time for

910 ^{231}Pa and ^{230}Th in different experiments. Partition coefficients used in CTRL follows

911 (Chase et al., 2002; Siddall et al., 2005). Both p-coupled and p-fixed versions are

912 enabled in CTRL, which yields identical results (discussed in section 4.1). Only p-

913 fixed version is enabled in Exp_1 and Exp_2. The residence time (τ) is for p-fixed

914 version in each experiment.

915

WATER COLUMN ACTIVITY	Holocene core-top $^{231}\text{Pa}/^{230}\text{Th}$
(Guo et al., 1995)	(Yu, 1994)
(Cochran et al., 1987)	(DeMaster, 1979)
(Nozaki et al., 1987)	(Bacon and Rosholt, 1982)
(Bacon and Anderson, 1982)	(Mangini and Diester-Hass, 1983)
(Bacon et al., 1989)	(Kumar, 1994)

(Huh and Beasley, 1987)	(Yang et al., 1986)
(Rutgers van der Loeff and Berger, 1993)	(Anderson et al., 1983)
(Nozaki et al., 1981)	(Anderson et al., 1994)
(Nozaki and Nakanishi, 1985)	(Ku, 1966)
(Mangini and Key, 1983)	(Ku et al., 1972)
(Nozaki and Horibe, 1983)	(Frank et al., 1994)
(Moore, 1981)	(Shimmiel et al., 1986)
(Nozaki and Yamada, 1987)	(Frank, 1996)
(Roy-Barman et al., 1996)	(Yong Lao et al., 1992)
(Nozaki and Yang, 1987)	(Francois et al., 1993)
(Moran et al., 1995)	(Anderson et al., 1990)
(Luo et al., 1995)	(Mangini and Sonntag, 1977)
(Colley et al., 1995)	(Schmitz et al., 1986)
(Scholten et al., 1995)	(Shimmiel and Price, 1988)
(Cochran et al., 1995)	(Yong-Liang Yang et al., 1995)
(Vogler et al., 1998)	(Müller and Mangini, 1980)
(Moran et al., 1997)	(Mangini and U., 1987)
(Edmonds et al., 1998)	(Scholten et al., 1995)
(Moran et al., 2001)	(Walter et al., 1997)
(Edmonds et al., 2004)	(Lippold et al., 2011)
(Okubo et al., 2007b)	(Lippold et al., 2012b)
(Coppola et al., 2006)	(Bradtmiller et al., 2007)
(Moran et al., 2002)	(Gherardi et al., 2005)
(Okubo et al., 2004)	(Gutjahr et al., 2008)
(Okubo et al., 2007a)	(Hall et al., 2006)
(Okubo et al., 2012)	(Lippold et al., 2011)
(Robinson et al., 2004)	(Roberts et al., 2014)
(Thomas et al., 2006)	(Bradtmiller et al., 2014)
(Trimble et al., 2004)	(Burckel et al., 2016)
(Venchiarutti et al., 2011)	(Hoffmann et al., 2013)
(Hsieh et al., 2011)	(Jonkers et al., 2015)
(Scholten et al., 2008)	(Negre et al., 2010)
(Luo et al., 2010)	
(Deng et al., 2014)	
(Hayes et al., 2013)	
(Hayes et al., 2015)	

916

917

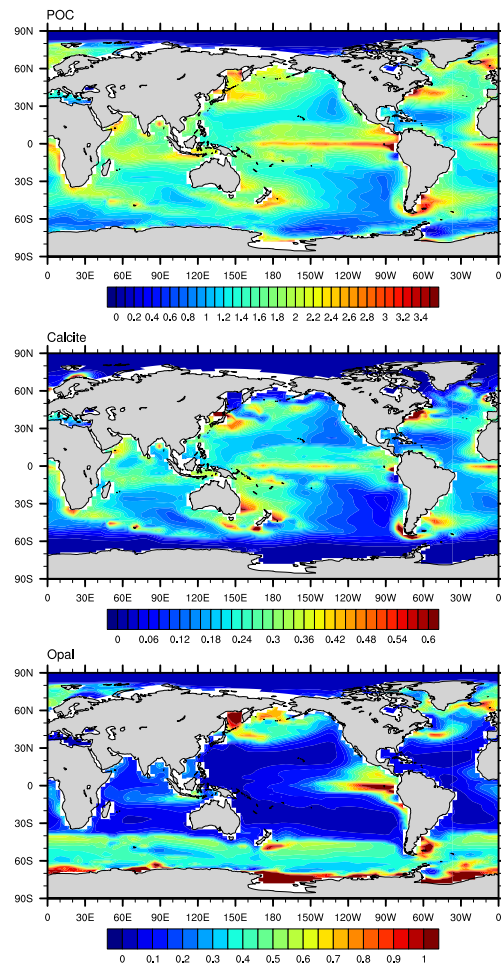
918 Table 3. References for observations of water column ^{231}Pa and ^{230}Th activity (left
919 column) and Holocene core-top $^{231}\text{Pa}/^{230}\text{Th}$ (right column).

920

921

922

923 Figures:

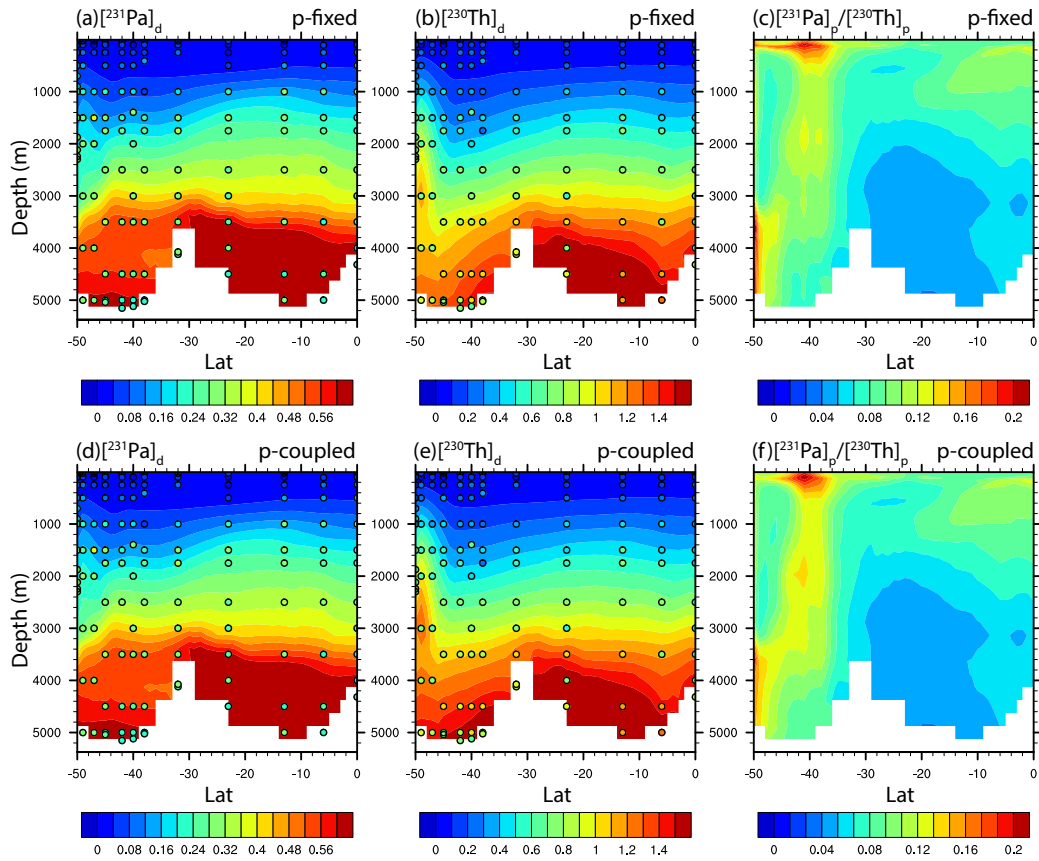


924

925 Figure 1. Annual mean particle fluxes in CESM. (a) CaCO_3 flux at 105m ($\text{mol m}^{-2} \text{yr}^{-1}$).

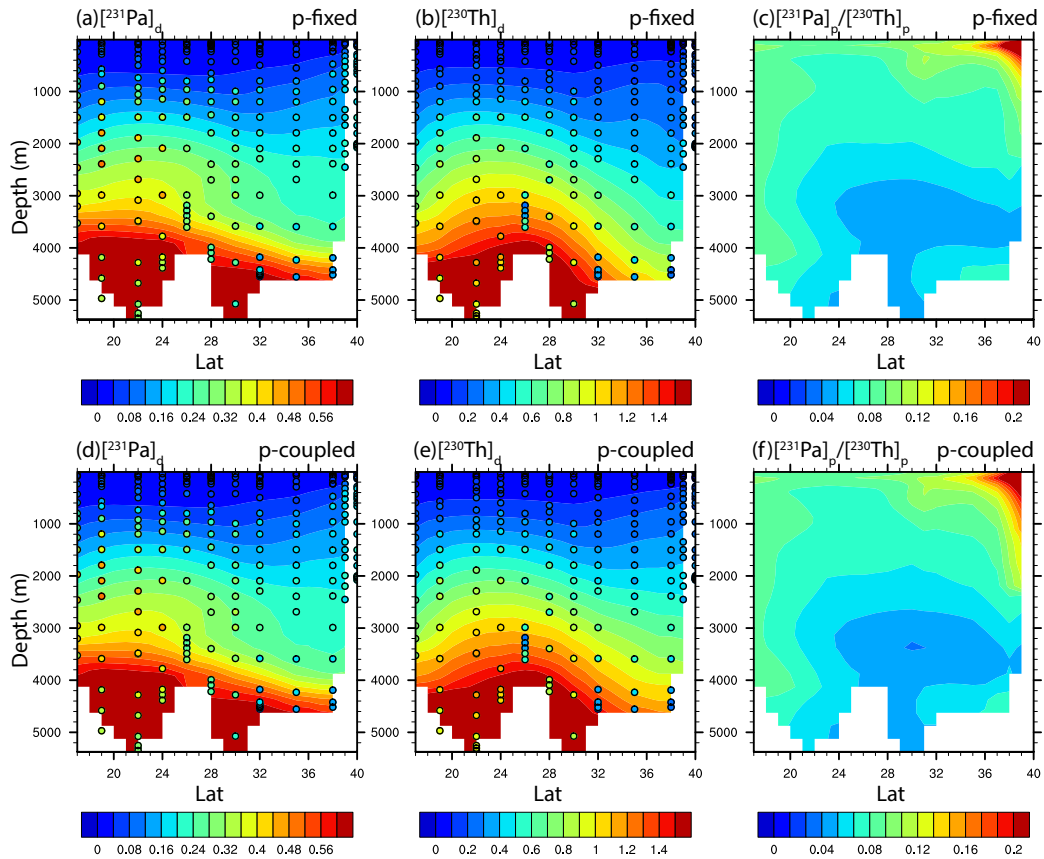
926 (b) Opal flux at 105m ($\text{mol m}^{-2} \text{yr}^{-1}$). (c) POC flux at 105m ($\text{mol m}^{-2} \text{yr}^{-1}$).

927

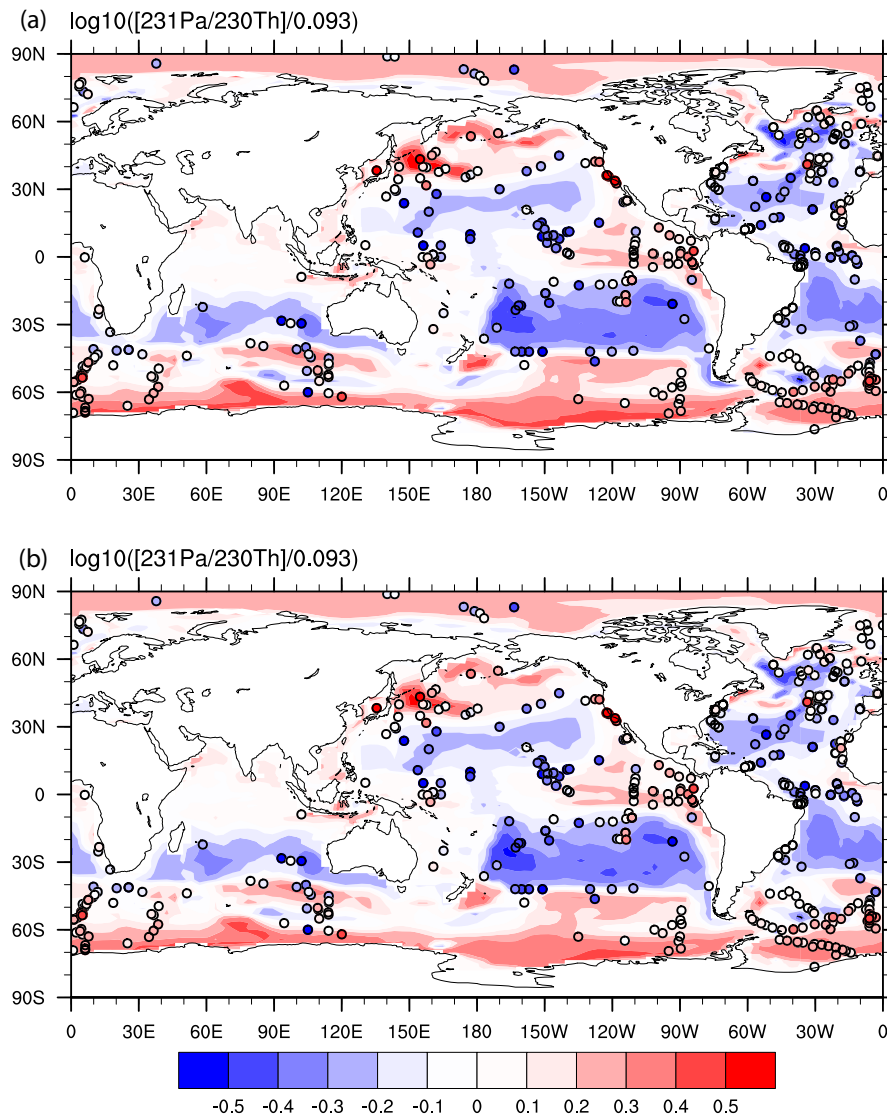


929

930 Figure 2. Dissolved ^{231}Pa , dissolved ^{230}Th and particulate $^{231}\text{Pa}/^{230}\text{Th}$ in CTRL along
 931 GEOTRACES transect GA02S (Deng et al., 2014) (the track is indicated in Fig. S4) for
 932 both p-fixed (top row) and p-coupled (bottom row) ^{231}Pa and ^{230}Th (colored
 933 contour). Observations of dissolved ^{231}Pa and ^{230}Th activity are superimposed as
 934 colored circles using the same color scale.



935
 936 Figure 3. Dissolved ^{231}Pa , dissolved ^{230}Th and particulate $^{231}\text{Pa}/^{230}\text{Th}$ in CTRL along
 937 GEOTRACES transect GA03 (Hayes et al., 2015) (the track is indicated in Fig. S4) for
 938 both p-fixed (top row) and p-coupled (bottom row) ^{231}Pa and ^{230}Th (colored
 939 contour). Observations of dissolved ^{231}Pa and ^{230}Th activity are superimposed as
 940 colored circles using the same color scale.



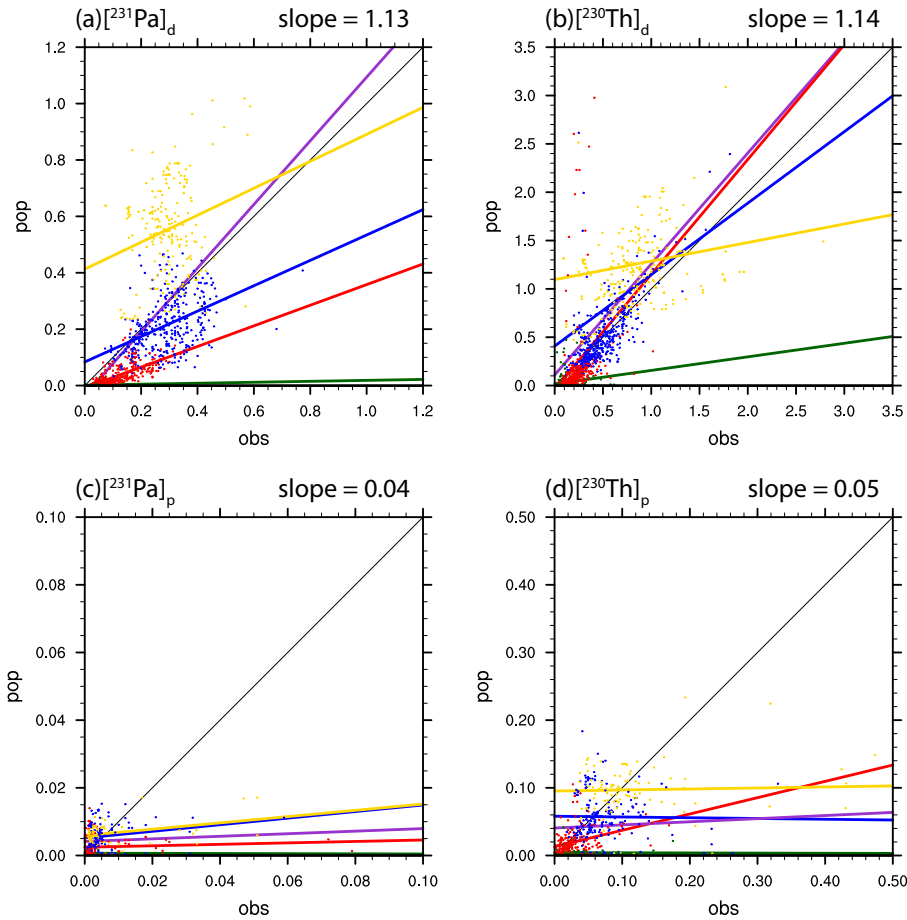
941

942 Figure 4. Sediment $^{231}\text{Pa}/^{230}\text{Th}$ activity ratio in CTRL for both p-fixed (a) and p-
 943 coupled version (b). Observations are attached as filled cycles using the same color
 944 map. The $^{231}\text{Pa}/^{230}\text{Th}$ activity ratio is plotted relative to the production ratio of
 945 0.093 on a \log_{10} scale.

946

947

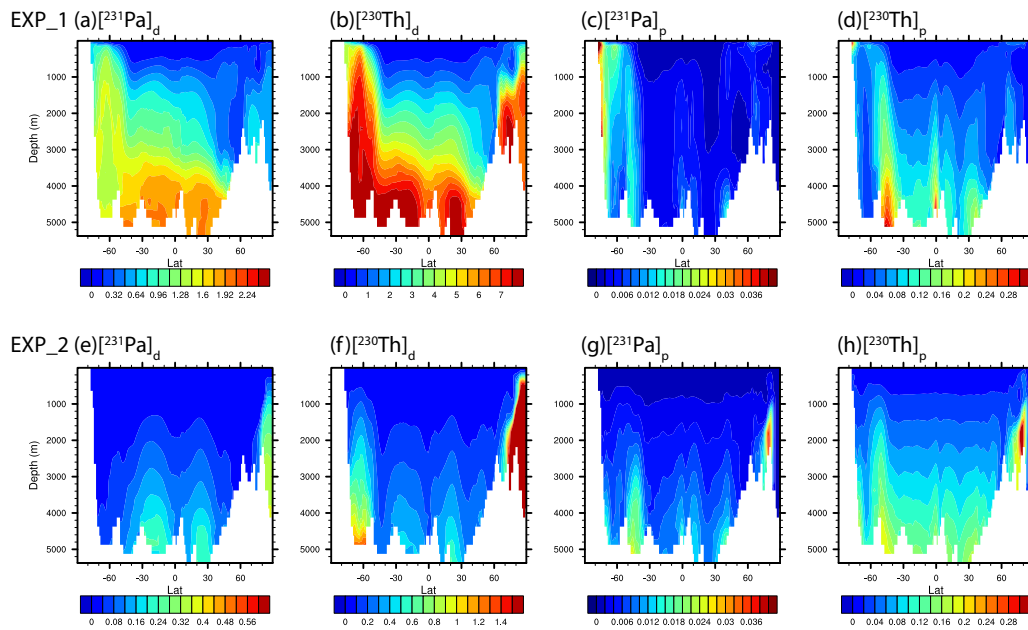
948



949

950

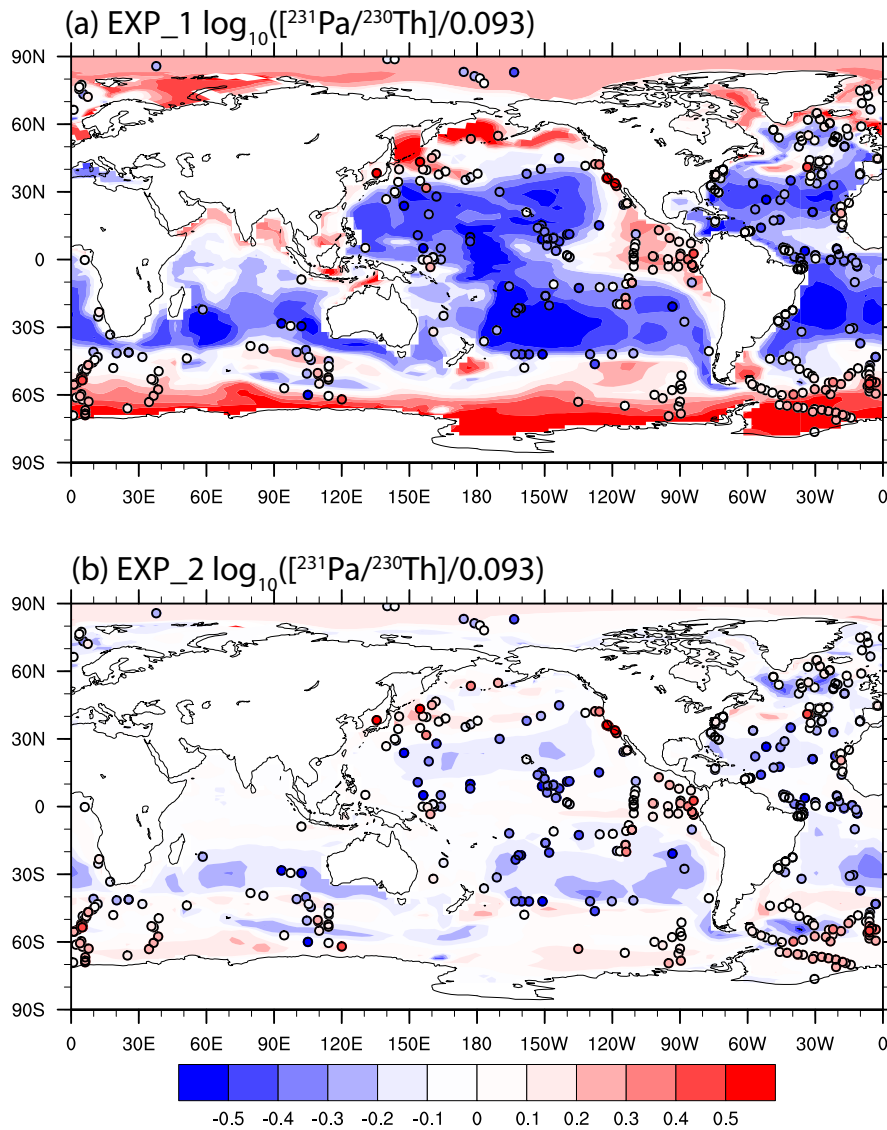
951 Figure 5. Scatter plot of global dissolved and particulate ^{231}Pa and ^{230}Th between
 952 observation and CTRL (p-fixed) (unit: dpm/m³). (a) dissolved ^{231}Pa ; (b) particulate
 953 ^{231}Pa ; (c) dissolved ^{230}Th ; (d) particulate ^{230}Th . Observations in different depth
 954 range are indicated by different colors: green for 0-100m; red for 100m-1,000m;
 955 blue for 1,000m-3,000m and yellow for deeper than 3,000m. Purple line is the least
 956 squared linear regression line for all depth range, the slope of which is indicated at
 957 the top right of each plot. Green line is the least squared linear regression line for
 958 depth from 0-100m. Red line is the least squared linear regression line for depth
 959 from 100m -1,000m. Blue line is the least squared linear regression line for depth
 960 from 1,000m-3,000m. Yellow line is the least squared linear regression line for
 961 depth deeper than 3,000m.



962

963 Figure 6. Atlantic zonal mean dissolved and particulate ^{231}Pa and ^{230}Th in EXP_1 and
 964 EXP_2 (unit: dpm/m^3). EXP_1: (a) dissolved ^{231}Pa ; (b) dissolved ^{230}Th ; (c)
 965 particulate ^{231}Pa ; (d) particulate ^{230}Th . EXP_2: (e) dissolved ^{231}Pa ; (f) dissolved
 966 ^{230}Th ; (g) particulate ^{231}Pa ; (h) particulate ^{230}Th .

967



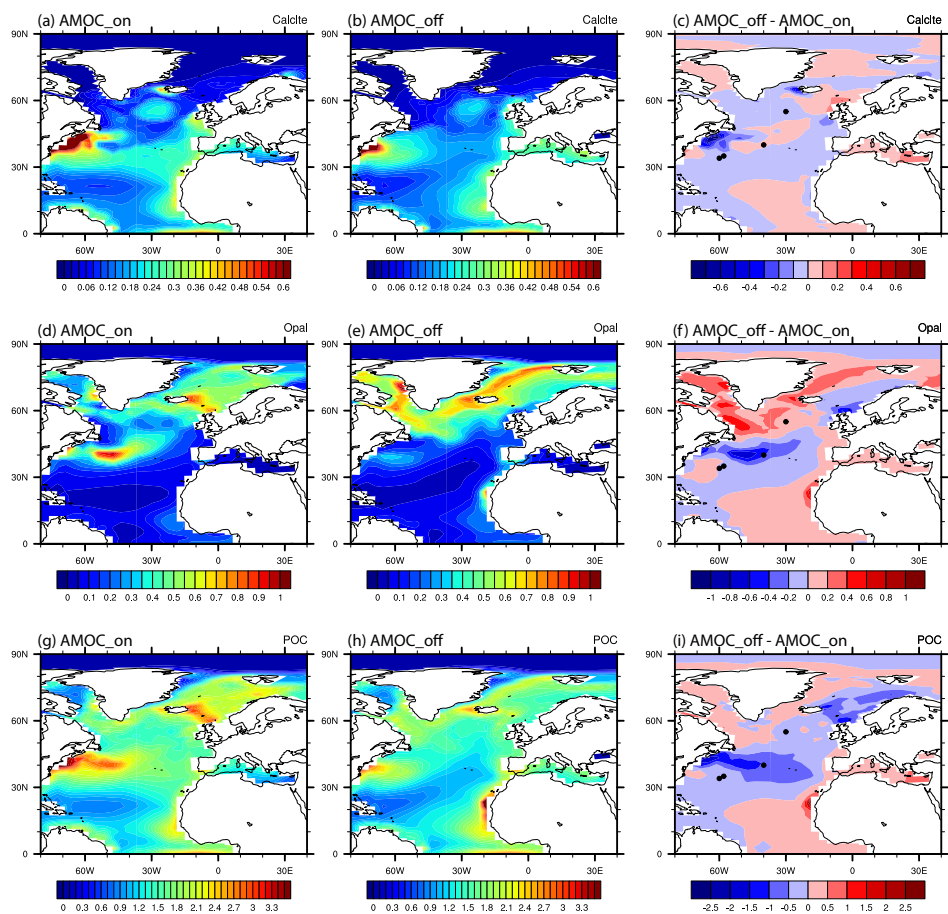
968

969 Figure 7. Sediment $^{231}\text{Pa}/^{230}\text{Th}$ activity ratio in EXP_1 (a) and EXP_2 (b).

970 Observations are attached as filled cycles using the same color map. The $^{231}\text{Pa}/^{230}\text{Th}$

971 activity ratio is plotted relative to the production ratio of 0.093 on a \log_{10} scale.

972

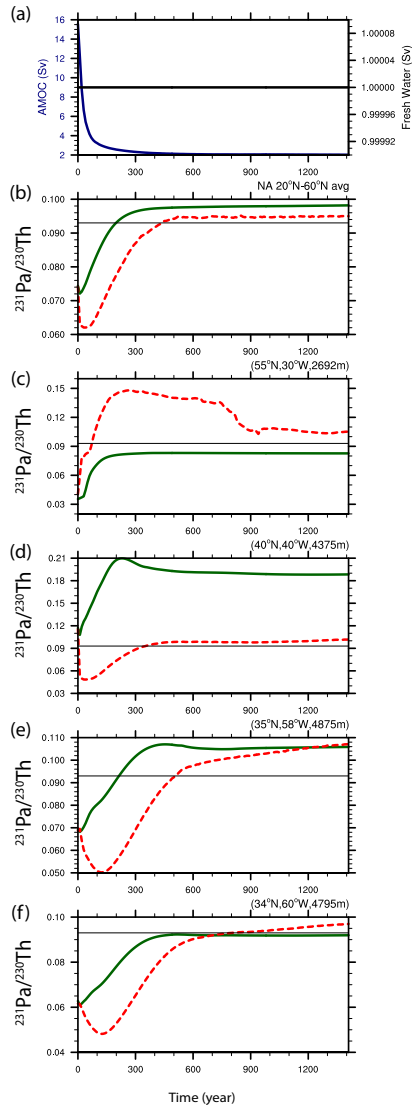


973

974 Figure 8. Comparison of particle fluxes between AMOC_on and AMOC_off. CaCO₃ flux
 975 at 105m (mol m⁻² yr⁻¹) during AMOC_on (a), AMOC_off (b) and difference between
 976 AMOC_off and AMOC_on. (b) Opal flux at 105m (mol m⁻² yr⁻¹) during AMOC_on (d),
 977 AMOC_off (e) and difference between AMOC_off and AMOC_on (f). POC flux at 105m
 978 (mol m⁻² yr⁻¹) during AMOC_on (g), AMOC_off (h) and difference between AMOC_off
 979 and AMOC_on (i).

980

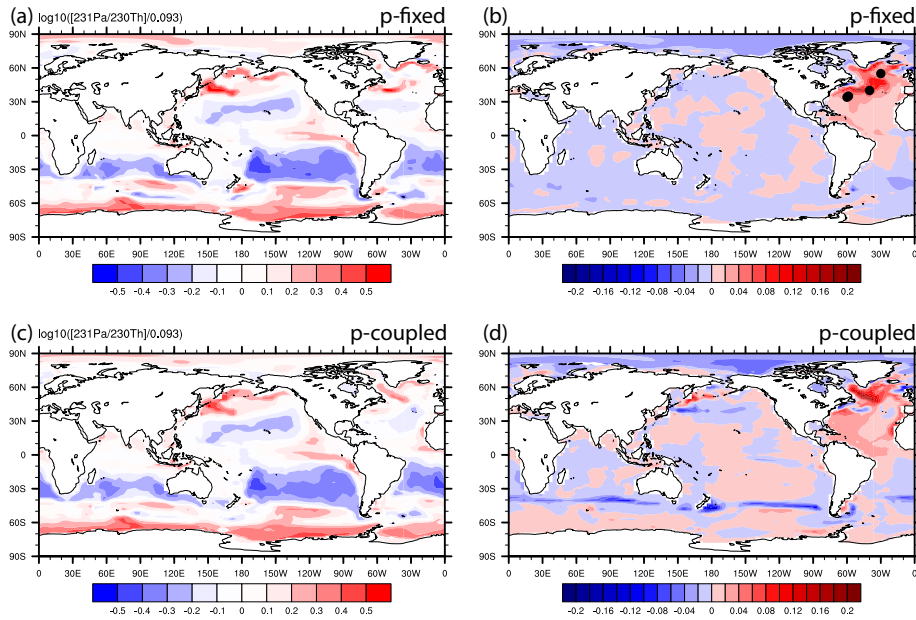
981



982

983

984 Figure 9. Time evolutions in HOSING. (a) Freshwater forcing (black) and AMOC
 985 strength (navy), which is defined as the maximum of the overturning
 986 streamfunction below 500m in the North Atlantic. (b) North Atlantic average
 987 sediment $^{231}\text{Pa}/^{230}\text{Th}$ activity ratio from 20°N to 60°N: p-fixed (green) and p-
 988 coupled (red). Production ratio of 0.093 is indicated by a solid black line (similar in
 989 c, d, e and f). (c) Sediment $^{231}\text{Pa}/^{230}\text{Th}$ activity ratio at (55°N, 30°W). (d) Sediment
 990 $^{231}\text{Pa}/^{230}\text{Th}$ activity ratio at (40°N, 40°W). (e) Sediment $^{231}\text{Pa}/^{230}\text{Th}$ activity ratio at
 991 (35°N, 58°W). (f) Sediment $^{231}\text{Pa}/^{230}\text{Th}$ activity ratio at (34°N, 60°W). (e) and (f) are
 992 near Bermuda Rise. Locations of each site are shown as dots in Fig. 8b.

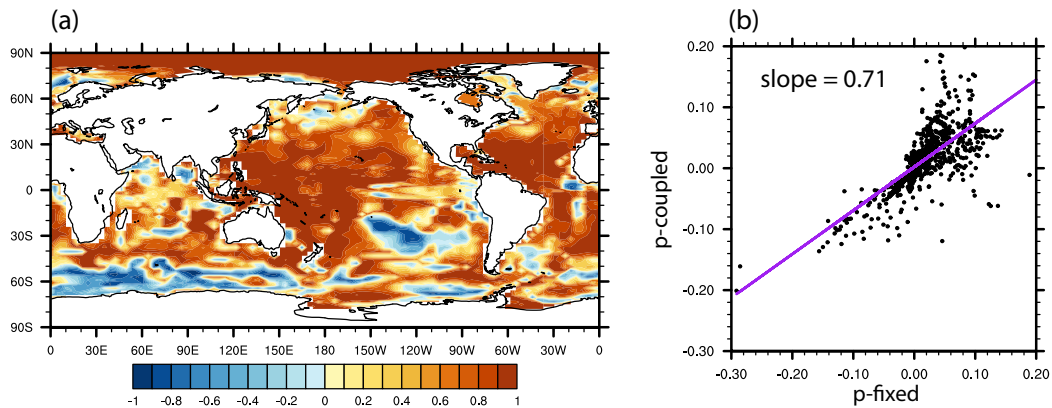


994

995

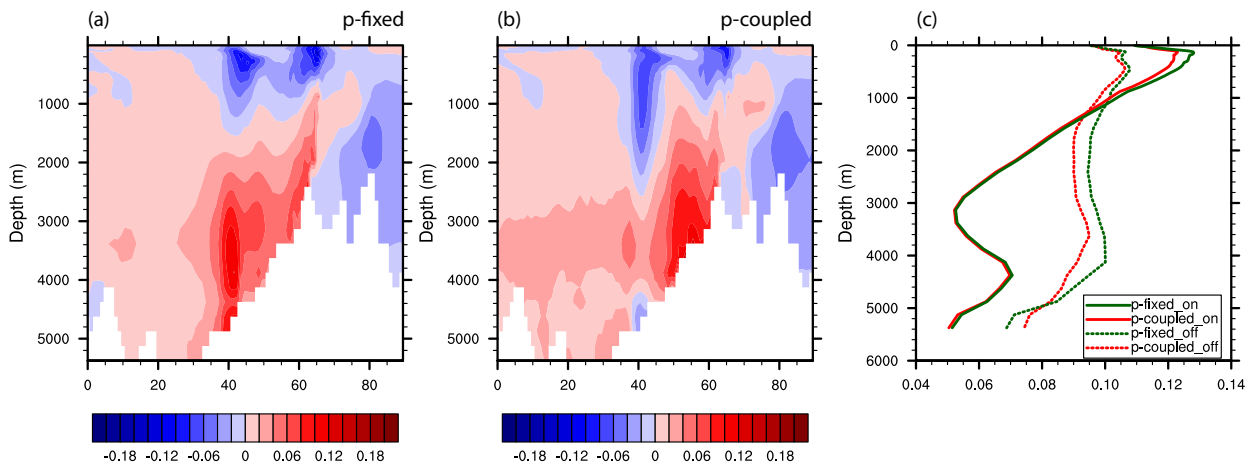
996 Figure 10. Sediment $^{231}\text{Pa}/^{230}\text{Th}$ activity ratio during AMOC off state and the
 997 difference between AMOC off and CTRL. (a) P-fixed $\log_{10}([^{231}\text{Pa}/^{230}\text{Th}]/0.093)$ in
 998 AMOC_off. (b) Difference of p-fixed sediment $^{231}\text{Pa}/^{230}\text{Th}$ activity ratio between
 999 AMOC_off and AMOC_on. (c) and (d) are similar to (a) and (b) for p-coupled
 1000 sediment $^{231}\text{Pa}/^{230}\text{Th}$ activity ratio. Black dots in (b) shows the locations of sites in
 1001 Fig. 9 from North to South.

1002



1003

1004 Figure 11. (a) Correlation of p-fixed and p-coupled evolution of sediment
 1005 $^{231}\text{Pa}/^{230}\text{Th}$ activity ratio in HOSING. (b) Scatter plot of p-fixed and p-coupled
 1006 sediment $^{231}\text{Pa}/^{230}\text{Th}$ activity ratio change from AMOC_on to AMOC_off in the
 1007 Atlantic and the Southern Ocean (70°W-20°E). Purple line is the least squared linear
 1008 regression line and slope is the linear regression coefficient.
 1009



1010
 1011 Figure 12. Difference of Atlantic zonal mean particulate $^{231}\text{Pa}/^{230}\text{Th}$ between
 1012 AMOC_off and AMOC_on: (a) p-fixed and (b) p-coupled. (c) North Atlantic (20°N-
 1013 60°N) average profile during AMOC_on (solid) and AMOC_off (dash) for p-fixed
 1014 (green) and p-coupled (red) particulate $^{231}\text{Pa}/^{230}\text{Th}$.
 1015
 1016
 1017
 1018